

Lyman α absorption beyond the disc of simulated spiral galaxies

Bernhard Röttgers,¹ Thorsten Naab^{1b},^{1★} Miha Cernetic^{1b},^{1★} Romeel Davé^{1b, 2,3,4},
Guinevere Kauffmann,¹ Sanchayeeta Borthakur⁵ and Horst Foidl⁶

¹Max-Planck-Institut für Astrophysik, Karl-Schwarzschild-Str 1, D-85748 Garching, Germany

²Institute for Astronomy, Royal Observatory, University of Edinburgh, Edinburgh EH9 3HJ, UK

³University of the Western Cape, Bellville, Cape Town 7535, South Africa

⁴South African Astronomical Observatories, Observatory, Cape Town 7925, South Africa

⁵School of Earth and Space Exploration, Arizona State University, 781 Terrace Mall, Tempe, AZ 85287, USA

⁶Department of Astrophysics, University of Vienna, Türkenschanzstr 17, A-1180 Wien, Austria

Accepted 2020 May 20. Received 2020 May 14; in original form 2020 March 17

ABSTRACT

We present an analysis of the origin and properties of the circumgalactic medium (CGM) in a suite of 11 cosmological zoom simulations resembling present-day spiral galaxies. On average the galaxies retain about 50 per cent of the cosmic fraction in baryons, almost equally divided into disc (interstellar medium) gas, cool CGM gas and warm-hot CGM gas. At radii smaller than 50 kpc the CGM is dominated by recycled warm-hot gas injected from the central galaxy, while at larger radii it is dominated by cool gas accreted on to the halo. The recycled gas typically accounts for one-third of the CGM mass. We introduce the novel publicly available analysis tool PYGAD to compute ion abundances and mock absorption spectra. For Lyman α absorption, we find good agreement of the simulated equivalent width (EW) distribution and observations out to large radii. Disc galaxies with quiescent assembly histories show significantly more absorption along the disc major axis. By comparing the EW and H I column densities, we find that CGM Lyman α absorbers are best represented by an effective line width $b \approx 50\text{--}70\text{ km s}^{-1}$ that increases mildly with halo mass, larger than typically assumed.

Key words: line: profiles – circumstellar matter – Galaxy: formation – quasars: absorption lines.

1 INTRODUCTION

Star-forming galaxies mostly grow by accreting gas from their surrounding medium, fuelling star formation (Kereš et al. 2005; Dekel et al. 2009). This accretion can include relatively pristine gas that has come directly from the intergalactic medium (IGM), or gas that was previously ejected from a galaxy, known as wind recycling (Oppenheimer et al. 2010), including potentially significant intergalactic transfer (Anglés-Alcázar et al. 2017). The circumgalactic medium (CGM) thus serves as a reservoir that holds signatures of accretion, outflows, and wind recycling, as well as holding the majority of baryons within haloes (Peeples et al. 2014; Tumlinson, Peeples & Werk 2017).

At present, the CGM is best probed using absorption line techniques. From H I and metal absorption studies around low-redshift galaxies, the CGM is found to be extended and highly multi-phase (e.g. Chen et al. 1998; Werk et al. 2014; Hafen et al. 2019, 2020) in a manner that depends on the host galaxy

properties (e.g. Tumlinson et al. 2011; Thom et al. 2012). It is likely to be dynamic, although it appears that absorber relative velocities rarely exceed the galaxy escape velocity (Tumlinson et al. 2013). These complex processes can be difficult to disentangle using only the one-dimensional spectral probes along a limited number of sightlines. For this reason, gas dynamical simulations are now commonly employed to help relate the observable absorption line properties with the physical and dynamical state of CGM gas (Ford et al. 2013, 2014).

Modelling the CGM represents a substantial computational challenge. To begin with, it is important to have a model that is able to produce realistic galaxy properties (Ford et al. 2013; Kauffmann, Borthakur & Nelson 2016; Gutcke et al. 2017; Nelson et al. 2018; Oppenheimer et al. 2018; Hafen et al. 2019). Only in recent years have groups succeeded in simulating realistic spirals, owing primarily to improvements in understanding of the impact of star formation feedback (see Somerville & Davé 2015; Naab & Ostriker 2017 for reviews), and numerical resolution afforded by advancing computing power. On a cosmological scale such models none the less make a wide range of predictions for CGM gas (Ford et al. 2016; Kauffmann et al. 2016; Nelson et al. 2018), owing to variations in feedback physics that, while constrained to reproduce

* E-mail: naab@mpa-garching.mpg.de (TN); cernetic@MPA-Garching.MPG.DE (MC)

the stellar component, can deposit widely varying amounts of mass, metals, and energy into the CGM. It is also not clear that current CGM simulations have achieved convergence (Kauffmann et al. 2019), even as clever techniques have been employed to enhance resolution specifically in the CGM (Hummels et al. 2019; Peeples et al. 2019; van de Voort et al. 2019). The CGM is thus a crucial test bed for modern galaxy formation models, and developing improved models for examining the role of the CGM in galaxy evolution remains an important goal.

In this paper, we examine the CGM physical conditions and associated absorption line properties in a suite of 11 zoom-in simulations of star-forming galaxies spanning from dwarfs to super- L^* . We employ a smoothed particle hydrodynamics (SPH)-based code that explicitly tracks the cold and hot ISM phases separately (Aumer et al. 2013). By tracking particles, we are able to quantify the origin of CGM gas, both pristine and enriched, in these simulations. We examine radial trends of absorption strength in various ions. Along the way, we introduce a new publicly available code to generate absorption line spectra called (PYGAD; Röttgers 2018),¹ which doubles as a general-purpose SPH simulation visualization and analysis tool.

This paper is organized as follows: in Section 2, we describe and briefly review the simulations. The bulk properties of the ISM and CGM are presented in Section 3. In Section 4, we describe our spectral line generation code, and in Section 5 we use this to study CGM absorption properties. We discuss feedback and resolution dependence in Section 6, and summarize in Section 7.

2 SIMULATIONS

2.1 Code description

The simulations are performed with the multiphase cosmological SPH implementation of GADGET (Springel 2005) presented in Aumer et al. (2013). It is a modified version of the code used by Scannapieco et al. (2006), Scannapieco et al. (2005) and is built on the TreeSPH code GADGET-3. The code includes models for a multiphase gas treatment, metal line cooling, star formation, stellar metal production and feedback, and a spatially homogeneous, redshift-dependent UV-background (Haardt & Madau 2001). With this implementation it is possible to successfully produce realistic present-day properties, like stellar sizes, kinematic stellar disc mass fractions, and H I sizes and evolution histories of the spiral galaxy population (Aumer et al. 2013; Aumer, White & Naab 2014; Übler et al. 2014; Wang et al. 2014). Here, we briefly describe the unchanged features of the code and in more detail the added improvements with respect to energy conservation in all feedback events, and the decoupling of the AGB feedback from the feedback of Type Ia supernovae (SNe). For further details we refer the reader to Aumer et al. (2013) and Scannapieco et al. (2005, 2006).

2.2 Multiphase gas model

From observations it is known that the interstellar gas has a complex structure with different phases – a hot volume-filling phase and a dense cold gas phase – both of which should be represented in galaxy formation simulations (see Naab & Ostriker 2017; Tumlinson et al.

2017). To model this, we treat the gas as a multiphase medium with many co-existing phases (see Marri & White 2003). We let two SPH particles i and j decouple into separate phases, if the following two conditions apply (Aumer et al. 2013):

$$\max\left(\frac{A_i}{A_j}, \frac{A_j}{A_i}\right) > 50, \quad -\mu_{ij} < c_{ij}. \quad (1)$$

Here, A_{ij} are the entropic functions of the particles (Springel & Hernquist 2002), $\mu_{ij} := (\mathbf{v}_i - \mathbf{v}_j) \cdot \frac{\mathbf{r}_i - \mathbf{r}_j}{|\mathbf{r}_i - \mathbf{r}_j|}$ is the relative velocity of the particles along their vector of separation, and c_{ij} is the pair-averaged sound speed. Two SPH particles decouple if their entropy (actually their entropic functions²) are very different unless they approach faster than with the local sound speed. The velocity restriction (equation 1) is required to capture shocks properly (Marri & White 2003). This multiphase treatment results in a continuum of phases from cold to hot and the results are not very sensitive to the exact ratio in equation (1). This model is aimed at preventing overcooling, i.e. artificially short cooling times (see e.g. Naab & Ostriker 2017, for a review) and allows for the simultaneous representation of, and energy injection into, a hot and a cold phase on the resolution scale (see Scannapieco et al. 2006, for a detailed discussion). Such multiphase ISM structure naturally arises in much higher resolution simulations of the supernova-driven multiphase ISM (see e.g. Walch et al. 2015). For further details on the multiphase model, see Marri & White (2003) and Aumer et al. (2013, 2014).

2.3 Star formation

Gas particles are converted into star particles stochastically such that on average they have a star formation rate of

$$\text{SFR} = \eta \frac{\rho_{\text{gas}}}{t_{\text{dyn}}} \left(\propto \rho_{\text{gas}}^{1.5} \right). \quad (2)$$

Here, ρ_{gas} is the gas density and $t_{\text{dyn}} \equiv (4\pi G \rho_{\text{gas}})^{-1/2}$ is the local dynamical time for the gas particle. This results in a Kennicutt–Schmidt like relation (Schmidt 1959; Kennicutt 1998) locally and the star formation efficiency η is set to a typical value of 0.04 (Aumer et al. 2013).

Gas is only allowed to form stars if the density fulfils the following conditions (Aumer et al. 2013):

$$n > n_{\text{th}} \simeq 3 \text{ cm}^{-3} \simeq 10^{-1} \text{ M}_{\odot} \text{ pc}^{-3}, \quad \frac{\rho}{\langle \rho \rangle} > 2000, \quad (3)$$

where $\langle \rho \rangle$ is the cosmic mean baryon density and n is the number density of the gas.

Each stellar particle spawned from the gas represents a stellar population with a Kroupa (2001) initial mass function in the range of 0.1 and 100 M_{\odot} .

2.4 Metal enrichment

2.4.1 Metal production

We follow enrichment and cooling for H, He, and nine metals: carbon, nitrogen, oxygen, neon, magnesium, silicon, sulphur, calcium, and iron, as they are produced by Type Ia, II supernovae as well as AGB stars. The SNe II yields are metal-dependent following Chieffi & Limongi (2004), but with the iron yield halved as proposed by

¹PYGAD is available at: <https://bitbucket.org/broett/pygad>. The legacy version used in this paper is in PYTHON 2. A PYTHON 3 version is available and will be maintained in the future.

²The entropic function A is defined by $P =: A(s)\rho^{\gamma}$, where P is the pressure, s is the specific entropy, ρ is the density, and γ is the adiabatic index.

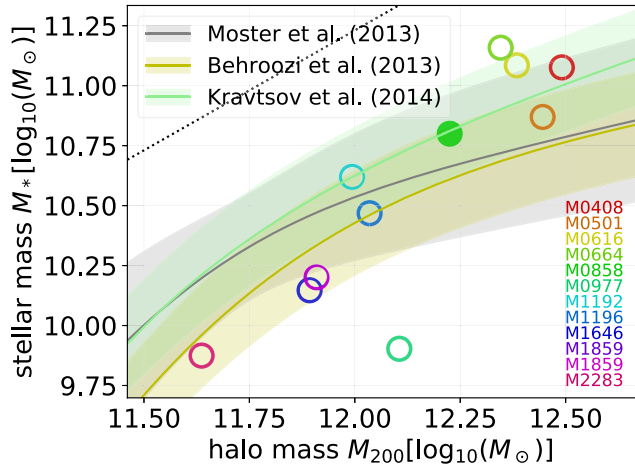


Figure 1. The stellar mass–halo mass relation for the simulated haloes at redshift zero. The example halo discussed in detail (M0858) is highlighted as a solid (green) circle. For reference, the abundance matching results from Kravtsov, Vikhlinin & Meshcheryakov (2018), Behroozi, Wechsler & Conroy (2013), and Moster, Naab & White (2013) are shown in differently coloured bands. With the exception of M0977, which is undergoing a major merger at $z = 0$ (see the text for more detail), all central galaxies agree with abundance matching constraints. At higher halo masses the simulated stellar masses are high, possibly due to missing black hole feedback. The dashed black line indicates the cosmic baryon fraction of the given halo.

Portinari, Chiosi & Bressan (1998). The element production by SNe Ia follows the W7 model of Iwamoto et al. (1999), with a declining rate by the inverse of the stellar population age sampled in time-steps of 50 Myr. We account for the mass recycling by AGB stars, with the same time sampling as for SNe Ia, by using the metal yields of Karakas (2010). In contrast to Aumer et al. (2013), we do not add the mass return of AGB stars to that of the supernovae but assume an outflow velocity of 30 km s^{-1} . This reduces the energy input by AGB winds, but does not change the results significantly (e.g. compare Fig. 1). The galaxies become smaller which is in better agreement with observations.

For the feedback we distinguish two different gas phases (again following Aumer et al. 2013), with a cold phase defined by $T < 8 \times 10^4 \text{ K}$ and $n > 4 \times 10^{-5} \text{ cm}^{-3}$, and the remaining gas in the hot phase. Note these phases are distinct from the range of phases used for hydrodynamics (cf. equation 1). Metals and energy/momentum from AGBs and SNe are returned separately into these two gas phases. In our implementation 50 per cent of the metals created in a supernova are deposited into the neighbouring hot phase, the other 50 per cent are deposited in the cold phase. We proceed in the same way for momentum and energy injection (see also Section 2.5.1). The motivation is that in the neighbourhood (i.e. within a kernel, that contains about $2.4 \times 10^7 M_\odot$, spread over at least $\sim 200 \text{ cpc } h^{-1}$ of a star, there is always unresolved hot and cold dense gas and any feedback event will typically deposit mass and energy into both phases. The exact ratios are unknown in nature. Aumer et al. (2013) found that the simple choice of 50:50 yields reasonable galaxies in terms of the global measures such as the stellar mass–halo mass relation.

2.4.2 Metal line cooling

As shown by Wiersma, Schaye & Smith (2009), cooling rates by metal lines with the correct element abundances are important for

a correct treatment in galaxy formation simulations. We implement their rates for optically thin gas in ionization equilibrium. This includes a redshift-dependent UV background of Haardt & Madau (2001) making the cooling rates dependent on redshift, density, temperature, and chemical composition.

2.4.3 Metal diffusion

We follow metal diffusion due to turbulent gas mixing with an SPH formulation of the diffusion equation ($\frac{dc}{dt} = \frac{1}{\rho} \nabla \cdot (D \nabla c)$ for some concentration c and a diffusion coefficient D). We do not simply use a discretized SPH formulation, but follow Greif et al. (2009), who argued for a version integrated over the small discrete time-step Δt of the simulation. To conserve (metal) mass, we use the same equation for the metal mass $\mu_i = c_i m_i$ of particle i as Aumer et al. (2013):

$$\begin{aligned} \Delta \mu_i &= \sum_j \mu_{i \rightarrow j} \\ &= \sum_j \left(\frac{1}{2} m_i (1 - e^{A \Delta t}) \frac{1}{A} K_{ij} (c_i - c_j) \right), \end{aligned} \quad (4)$$

where the sum goes over all SPH neighbours j of particle i , m_i is the i th particle’s mass, $A \equiv \sum_j K_{ij}$, and

$$K_{ij} = \frac{m_j}{\rho_i \rho_j} \frac{4 D_i D_j}{D_i + D_j} \frac{\mathbf{r}_{ij} \cdot \nabla_i W_{ij}}{r_{ij}^2}. \quad (5)$$

Here, $\rho_{i,j}$ are the respective particle densities, W_{ij} is the kernel of particle i at the position of particle j , and \mathbf{r}_{ij} is the separation vector of the two particles.

Finally, we choose the diffusion coefficients D_i as proposed by Shen, Wadsley & Stinson (2010), which does not introduce diffusion in purely rotational or compressive flows due to the use of the trace-free tensor S_{kl} (see their paper for details):

$$D_i = 0.05 \rho_i |S_{kl}| h_i^2, \quad (6)$$

where h_i is the smoothing length of particle i . Aumer et al. (2013) found that this coefficient also yields better agreement with observational data, such as the mass–metallicity relation, when applied in cosmological galaxy formation simulations than the one proposed by Greif et al. (2009).

2.5 Stellar feedback

We consider thermal and kinetic feedback from SNe II, SNe Ia, and winds from AGB stars. In this section, we describe how the feedback is modelled, and the modifications to Aumer et al. (2013). We also briefly describe the additional approximation to radiative feedback from O and B stars.

2.5.1 Thermal and kinetic feedback

We assume that each SN injects 10^{51} erg into the surrounding ISM. Each of the 10 nearest hot and cold neighbours receive the momentum corresponding to an outflow velocity of 3000 km s^{-1} pointing radially away from the stellar population particle. The transferred momentum changes the kinetic energy of the receiving gas particle. Assuming inelastic collisions, the remaining energy is added as thermal energy to ensure energy conservation. The thermal energy is not added to particles of the hot phase, but put into a reservoir for cold phase particles (using the definition

Table 1. Overview of the simulated haloes at redshift $z = 0$ used for this study. The naming (IDs) is taken from Oser et al. (2010, 2012) and is identical to Aumer et al. (2013). R_{200} is the radius around the galaxy where the mean spherical overdensity drops below $200 \rho_{\text{crit}}$ and M_{200} is the mass within. M_* is the stellar mass within 10 per cent of R_{200} . Gas fractions (f_{gas}), metallicity (Z_{gas}), and hydrogen mass ($M_{\text{H I}}$) are also taken within that radius. $R_{\text{H I}}$ is the size of the H I disc, defined as the radius at which surface density of H I falls below $1 \text{ M}_{\odot} \text{ pc}^{-2}$. The mass of the CGM (M_{CGM}) is measured within R_{200} (see the text) and $f_{\text{CGM}}^{\text{accreted}}$ is the CGM mass fraction which is accreted on to the halo from the outside. Galaxies with ongoing (major) galaxy mergers are in parentheses and are excluded from the analysis.

Halo ID	R_{200} (kpc)	M_{200} ($10^{12} \text{ M}_{\odot}$)	M_* ($10^{11} \text{ M}_{\odot}$)	f_{gas} (per cent)	Z_{gas} (Z_{\odot})	$M_{\text{H I}}$ ($10^{10} \text{ M}_{\odot}$)	$R_{\text{H I}}$ (kpc)	M_{CGM} ($10^{11} \text{ M}_{\odot}$)	$f_{\text{CGM}}^{\text{accreted}}$ (per cent)	Late merger history
M0408	295	3.10	1.19	21.6	2.36	2.12	25	1.56	72.8	Saller, $z \approx 0.3$
M0501	285	2.79	0.74	16.7	1.94	1.01	62	1.07	67.2	Large, $z \approx 0.9$
M0616	272	2.42	1.22	20.7	3.02	1.78	17	1.31	70.0	Smaller, $z \approx 0.05$
(M0664)	264	2.22	1.44	7.2	2.72	0.45	10	1.08	84.2	Ongoing major
M0858	241	1.68	0.63	22.4	2.16	1.15	17	0.70	65.3	Small fly-by, $z \approx 0.1$
(M0977)	220	1.27	0.08	55.9	0.50	0.69	45	0.82	86.2	Ongoing major
M1192	201	0.99	0.42	22.2	2.01	0.81	20	0.22	70.9	Smaller, $z \approx 0.2$
M1196	208	1.08	0.29	26.9	1.43	0.76	25	0.30	74.9	Large, $z \approx 0.4$
(M1646)	186	0.78	0.14	43.8	1.04	0.75	20	0.28	77.3	Small fly-by, $z \approx 0.1$
M1859	189	0.81	0.16	36.4	1.05	0.64	25	0.15	73.2	Small, $z \approx 0.5$
(M2283)	153	0.43	0.07	32.8	0.81	0.23	11	0.16	64.2	Ongoing major

Table 2. Overview of the different resolutions levels in the zoom region. The baryonic masses are initial masses, since gas particles can later vary by a factor ~ 2 as they accumulate mass from stellar feedback and metal diffusion.

Level	Softening length (cpc h_0^{-1})		Particle masses (M_{\odot})	
	Baryons	Dark matter	Baryons	Dark matter
2x	400	900	5.9×10^6	2.9×10^7
4x	200	450	7.4×10^5	3.6×10^6
8x	100	225	9.2×10^4	4.5×10^5

in Section 2.2). Once the reservoir energy is sufficient to heat (‘promote’) the particle to the hot phase, it is released (i.e. added to the thermal energy). For a more detailed description we refer to Aumer et al. (2013).

2.5.2 Radiation pressure

Based on Hopkins, Quataert & Murray (2011), the stellar populations deposit a momentum of

$$\dot{p}_{\text{TP}} = (1 + \tau_{\text{IR}}) \frac{L_{\text{UV}}}{c}, \quad (7)$$

to the 10 nearest neighbours as a continuous force acting over the first 30 Myr in the life cycle of a stellar population particle. Here, L_{UV} is the UV luminosity, c is the speed of light, and τ_{IR} is the infrared optical depth. The latter is modelled by

$$\tau_{\text{IR}} = \tau_0 \times \max \left(1, \frac{\rho h}{\rho_{\text{sf}} h_{\text{sf}}} \right) \times \left(\frac{Z}{Z_{\odot}} \right) \times \min \left(\left(\frac{\sigma}{\sigma_0} \right)^3, 4 \right), \quad (8)$$

i.e. scaling with the local metallicity Z , the particle’s surface density approximated by its density ρ times its smoothing length h (limited by the star-forming surface density threshold $\rho_{\text{sf}} h_{\text{sf}}$), and the surrounding velocity dispersion σ cubed. The parameters used are $\tau_0 = 25$ and $\sigma_0 = 40 \text{ km s}^{-1}$. Additionally, the factor of $(\sigma/\sigma_0)^3$ is limited to 4, in order to avoid overly strong forces. This relatively strong radiation pressure feedback helps dispersing dense star-forming regions and results in formation histories and final stellar masses in agreement with observations (cf. also fig. 1 of Aumer et al. 2013).

2.6 The simulation sample

We simulated a suite of 11 zoomed-in cosmological simulations in a box of $(100 \text{ cMpc})^3$, from the parent dark matter-only simulation described in Oser et al. (2010). It was run with a flat Λ cold dark matter cosmology with $H_0 = 72 \text{ km s}^{-1} \text{ Mpc}^{-1}$, $\Omega_{\Lambda} = 0.74$, $\Omega_{\text{matter}} = 0.26$, $\Omega_{\text{baryon}} = 0.044$, $\sigma_8 = 0.77$, and $n_s = 0.95$.

For the zoom simulations we use the same initial conditions (ICs) and naming convention as Oser et al. (2010) and Aumer et al. (2013). We restrict ourselves to ICs of haloes with present-day virial masses in the range of $M_{200} \in [4 \times 10^{11} \text{ M}_{\odot}, 3 \times 10^{12} \text{ M}_{\odot}]$. This corresponds to stellar masses in the range from 7.5×10^9 to $1.2 \times 10^{11} \text{ M}_{\odot}$ (cf. Fig. 1).

With the minor changes to the original code of Aumer et al. (2013), the key properties of the galaxies do not change significantly. As an example we show the stellar mass-halo mass relation at $z = 0$ (see Fig. 1). Except for halo M0977, all central galaxies fall well into the region for stellar masses expected from abundance matching results. M0977 is in a late major merger stage and its stellar mass is about to double from $8 \times 10^9 \text{ M}_{\odot}$ to $1.4 \times 10^{10} \text{ M}_{\odot}$.

The galaxies in the most massive haloes ($> 2 \times 10^{12} \text{ M}_{\odot}$) of our ensemble have a tendency towards higher stellar masses, which might be attributed to the absence of supermassive black holes and the feedback of active galactic nuclei (see e.g. Somerville & Davé 2015; Naab & Ostriker 2017).

The galaxies have large dynamical stellar disc mass fractions as listed in Table 1, ranging from about one-third to more than 80 per cent. Among these values, Table 1 lists other key features of the galaxies at redshift zero such as the H I disc size, which is of interest for us as we investigate Lyman α absorption. For details on the H I disc sizes, see Section 4.1. The gas-phase metallicities of ongoing major mergers can become very low due to merger-driven metal-poor inflow (see e.g. Peeples, Pogge & Stanek 2009). These systems are excluded from the analysis. The calculation of these quantities is discussed in Sections 2.7 and 4.1. As an example of our simulations we show the structure of halo M0858 in Fig. 2, the halo which we will also discuss in more detail as an example in the following. We will discuss and use this halo as an example in this work.

We performed simulation at three different spatial resolutions which are referred to as ‘2x’, ‘4x’, and ‘8x’ (see Table 2). If not stated otherwise, we use the intermediate resolution ‘4x’. For ‘4x’

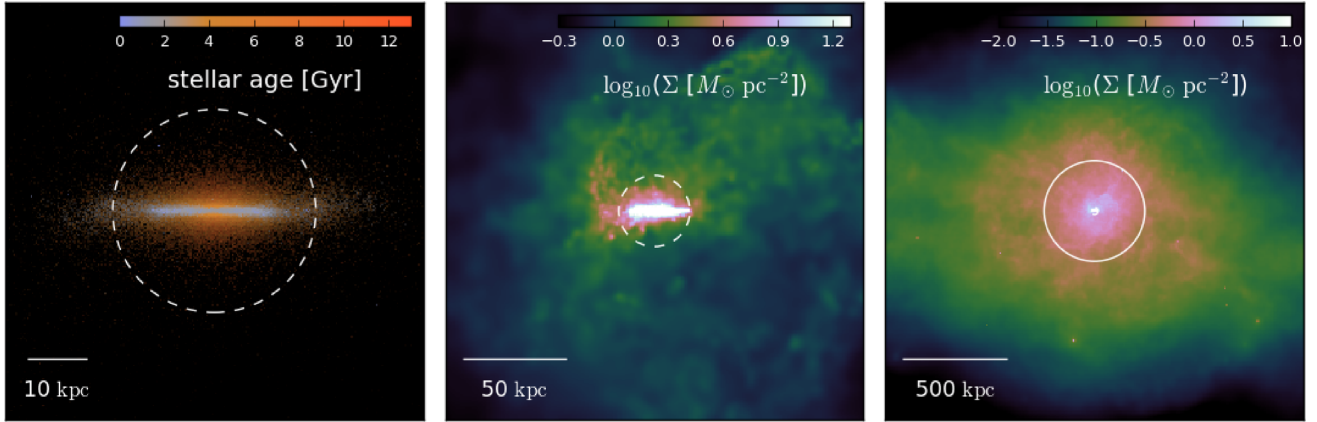


Figure 2. Morphological impression of galaxy M0858. In the left-hand panel, we show (edge-on) the stellar V-band luminosities (determining the pixel brightness / the value in HSV colour space), colour coded by the mean (V-band weighted) stellar ages (determining the pixel hue). The galaxy has a thin and young stellar disc. The middle panel displays the gas column density distribution in and around the galaxy. In the right-hand panel, we show the gas distribution beyond the galaxies’ virial radius (R_{200}), which is indicated by the solid circle. The dashed circles in the other panels is at the H I disc size, R_{HI} . The respective spatial scales are given in the lower left corner of the panels.

the (initial) gas particle mass is $7.4 \times 10^5 M_\odot$ and the gravitational softening length is $200 \text{ cpc}/h_0$.

2.7 Simulation analysis

All data analysis presented in this paper is performed with the publicly available, modular analysis tool PYGAD.

We identify the main haloes and their largest galaxies of the high-resolution part of the zoom simulations with a friends-of-friends algorithm. The simulation snapshots are then centred on the main galaxies of these haloes, using a shrinking sphere method (Power et al. 2003) on the stars. We calculate the spherical overdensity mass M_{200} and radius R_{200} of the dark matter haloes with respect to this centre. All baryons within 10 per cent of R_{200} are defined as galaxies (following Oser et al. 2010).

For rotating the systems to the edge-on projection we use the eigenvectors of the reduced moment-of-inertia tensor (Gerhard 1983; Bailin & Steinmetz 2005) of the galaxies, which are typically dominated by the stars as the mean gas fraction is close to 20 per cent (cf. Table 1). The z -axis is then aligned with the minor axis and the x -axis along the major axis of the galaxies.

3 ISM AND CGM BULK PROPERTIES

3.1 Mass budget

The sum of observed mass components within galaxy haloes has long been known to fall short of the expected cosmic baryon fraction, known as the missing halo baryon problem. It has been suggested that the shortfall lies in multiphase CGM gas, which has been difficult to quantify. Werk et al. (2014) used COS-Halos and other data to estimate the cool and warm-hot CGM components within $\sim 10^{12} M_\odot$ haloes to be 30–50 per cent and 5–40 per cent, respectively, with about 20 per cent in the ISM. In contrast, Stern et al. (2016) determined a data-concordant universal CGM density profile and estimated 5–10 per cent of the baryons in the cool CGM phase.

We compare our simulations with these estimates. We define gas within 15 per cent of R_{200} , $T < 2 \times 10^4 \text{ K}$, and $n_{\text{H}} > 10^{-2} \text{ cm}^{-3}$ as ISM gas (note that this might include the ISM of close satellites). The estimate for ‘disc’ then includes ISM gas and

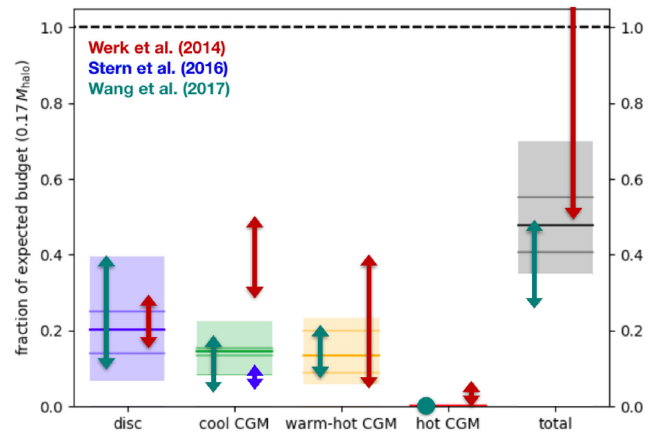


Figure 3. The mass budget of the haloes and the CGM in the simulations in a similar fashion as done by Werk et al. (2014) (indicated with red arrows here). Note that there are different measurement from Stern et al. (2016) and Wang et al. (2017) for cool gas in better agreement with our results. ‘disc’ is all stars and the ISM gas in the haloes; ‘cool CGM’ is all remaining gas with $T < 10^5 \text{ K}$; ‘hot-warm CGM’ gas has temperatures of $10^5 \text{ K} \lesssim T \lesssim 10^7 \text{ K}$; and ‘hot CGM’ finally is gas with $T > 10^7 \text{ K}$. The shaded region indicates the range of fractions found in the simulations. The median is marked with a thick line and the 25 and 75 percentiles are shown by the thin lines.

the stellar component of the galaxy. Remaining gas within R_{200} is considered CGM gas, divided into cool ($T < 10^5 \text{ K}$), warm-hot ($10^5 \text{ K} < T < 10^7 \text{ K}$), and hot ($10^7 \text{ K} < T$) components. The results for our simulation suite is shown in Fig. 3 compared to observational estimates from Werk et al. (2014) and Stern et al. (2016). The lightly shaded region shows the full range among the 11 zooms, with the median indicated by the thick horizontal line and the 25–75 per cent region shown by the thin lines.

We find 20 per cent in the ISM, in agreement with observational determinations. The fraction in the cool and warm-hot CGM are slightly lower but similar at 15–25 per cent each. This results in a total baryon fraction of about 50 per cent of the expected baryon fraction, with the rest having been expelled outside the halo. Our results are generally in agreement with observations, although the cool CGM estimate of Werk et al. (2014) is clearly higher; our

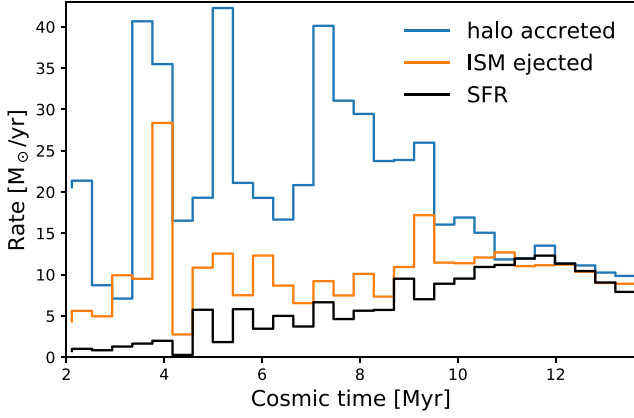


Figure 4. The instantaneous accretion and ejection histories of the CGM gas of M0858 over cosmic time. Orange-blue is gas crossing R_{200} on its way into the halo and becoming part of the CGM. The blue-orange histogram shows gas ejected from the ISM (see the text for details) into the CGM. The star formation rate in the galaxy (within 10 per cent of R_{200}) is shown in black. At late cosmic times the star formation and ejection rate becomes comparable.

results are in somewhat better agreement with Stern et al. (2016). For comparison, we also show the NIHAO simulation results from Wang et al. (2017), which are generally similar to ours.

In summary it appears that modern galaxy formation models that reproduce the stellar-to-halo mass relation result in significant

expulsion of gas from haloes, and result in baryons being roughly equally divided between the ISM, the cool CGM, and the warm-hot CGM. This is broadly concordant with observations, though the uncertainties remain substantial.

3.2 Particle tracing and CGM gas history

An interesting question is, how was the CGM assembled? Part of it comes from accretion on to the halo, while some of it may arise from material ejected from the ISM. To examine this, we take a prototypical galaxy from our sample, M0858, and trace the individual gas particles in time to examine the relative contribution from these two channels.

Fig. 4 shows the instantaneous accretion rate into the CGM of M0858 from halo accretion (orange-blue) and from material returned from the ISM (blue-orange). After the early stochastic growth phase, the halo accretion tends to dominate the contribution to the CGM. Occasional small mergers are seen as spikes in the halo accretion rate. At late times, when the star formation and hence feedback strength drops, there is an increase in the contribution from winds ejected from the ISM. The ISM ejection rate rises with the star formation rate and both rates settle at a few solar masses per year at present and the halo accretion rate has dropped to a similar level. Overall halo accretion dominates the build-up of the CGM.

A more detailed view of CGM growth in M0858 – which is typical for all galaxies in our sample – is provided by examining the temperature at infall. Fig. 5 shows a contour plot of the temperature of the gas at the time of infall (for halo accretion) or ejection

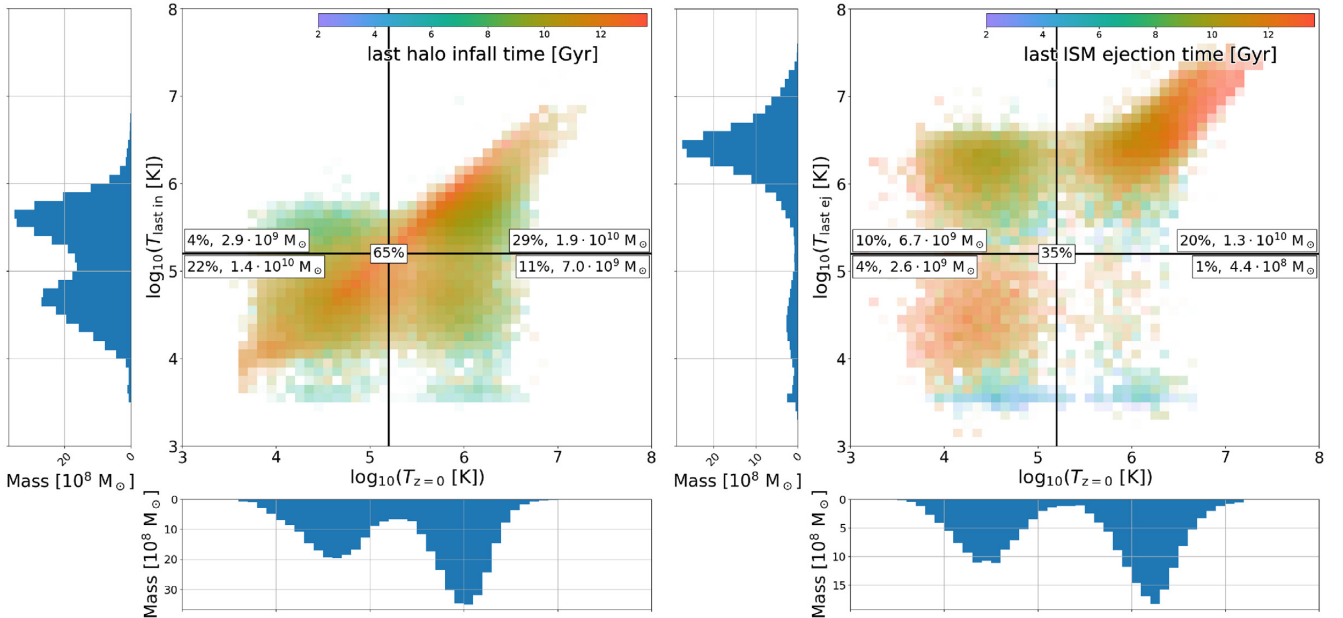


Figure 5. The temperature distribution of the CGM gas for M0858 at $z = 0$ separated into its origin. All percentages are given with respect to the total CGM mass. We have tracked the temperature of each gas phase element at infall time on to the halo ($T_{\text{last in}}$, left) and temperature at last ejection from the galaxy into the halo ($T_{\text{last ej}}$, right) and compare to the temperature at present $T_{z=0}$. Temperature ranges are separated into cold and hot by the thermally unstable regime ($\sim 10^{5.2}$ K). Gas accreted on to the halo, which has never been part of the central galaxy (left) makes up 65 per cent of the CGM gas. This gas is separated into four accretion to present-day transitions: hot-hot (29 per cent), hot-cold (4 per cent), cold-cold (22 per cent), and cold-hot (11 per cent). Most (22 per cent + 29 per cent of all CGM) of the halo accreted gas falls on to the halo within the last Gyr (left, red shaded region, see also Fig. 4) and did not change its temperature. Only 4 per cent was accreted hot and has cooled down and 11 per cent was accreted cold and has been heated up. Gas ejected from the ISM of the central galaxies account for 35 per cent of the total CGM (right). It is separated into four last ejection to present-day transitions: hot-hot (20 per cent), hot-cold (10 per cent), cold-cold (5 per cent), and cold-hot (1 per cent). The ejected gas is mostly hot (30 per cent) and a third of it has cooled down. The ejected CGM component is also dominated by recent events (red shading, see also Fig. 4). This diagram shows histories which are typical for all simulated galaxies in this paper.

(for ISM return) on the y-axis, relative to the temperature in the CGM at $z = 0$ along the x-axis. Histograms of each are shown along the sides. Black lines are shown at $T = 10^{5.2}$ K as a by-eye division between the cold and warm-hot phases (i.e. at the minimum in between the two histogram peaks). The percentages of total CGM gas in each quadrant are indicated as well as the respective masses.

Overall, about two-thirds (65 per cent) of the gas is halo accreted, while approximately one-third (35 per cent) of CGM comes from ISM ejection. The domination of halo accreted gas is typical for all our simulated systems (see $f_{\text{CGM}}^{\text{accreted}}$ column in Table 1. This is qualitatively consistent with the very detailed tracking analysis of Hafen et al. (2020) based on zoom simulations (five zooms in our mass range) with the FIRE II feedback implementation. In general, material that entered the CGM hot remains hot and similarly for the cold component; however, about 10 per cent of the CGM comes from gas that was accreted cold but ended up hot, and another 10 per cent from mass ejected from the ISM hot but ended up cold. There is a strong tendency for hot ISM ejected gas to remain hot in the CGM; cold ISM injection tends to be subject to rapid recycling as it cannot support itself thermally against gravity. For the halo accretion, both hot and cold accretion end up about equally contributing to the CGM, and there is only a weak trend for that gas being further heated. As a result, cold CGM gas predominantly comes from cold halo accretion, although hot ISM injection that subsequently cools provides a non-trivial contribution. These results highlight the interplay between halo heating, ISM energy injection, and subsequent CGM cooling and heating processes in setting the phase structure of the CGM.

In Fig. 6, we show the average radial distribution of the CGM gas in all simulations separated in temperature below and above $10^{5.2}$ K at $z = 0$. The cooler gas (upper panel) is clearly concentrated towards the central parts (< 75 kpc) whereas hot gas dominates at larger radii. In the lower two panels gas is separated into recycled gas ejected which in the past experienced at least one ejection from the central galaxies (middle panel) and non-recycled CGM gas which has only been accreted on to the halo and had never been in contact with the ISM (bottom panel). At radii larger than 50 kpc CGM gas is dominated by non-recycled gas accreted on to the halo, possibly enriched and heated in infalling galaxies, but mostly unaffected by feedback events in the central galaxy. The central 50 kpc are dominated by recycled gas. The central dominance of recycled gas in our simulations is significantly stronger than for the simulations analysed in Hafen et al. (2020), who use a different feedback model.

4 MOCK ABSORPTION SPECTRA

We will now examine how the CGM of our simulation suite appears when observed in absorption lines. We generate mock absorption spectra. Below we describe various approaches to mock absorption spectra generation in PYGAD analysis package and discuss the results.

4.1 Ionization fractions and H I

To create absorption line spectra, we must calculate the ionization fraction for the ion of interest. Given density, temperature, and a photoionizing background (Haardt & Madau 2001), the ionization fractions in the optically thin approximation can be calculated using CLOUDY (Ferland et al. 2013). We have not explored different estimates for the photoionizing background in this work.

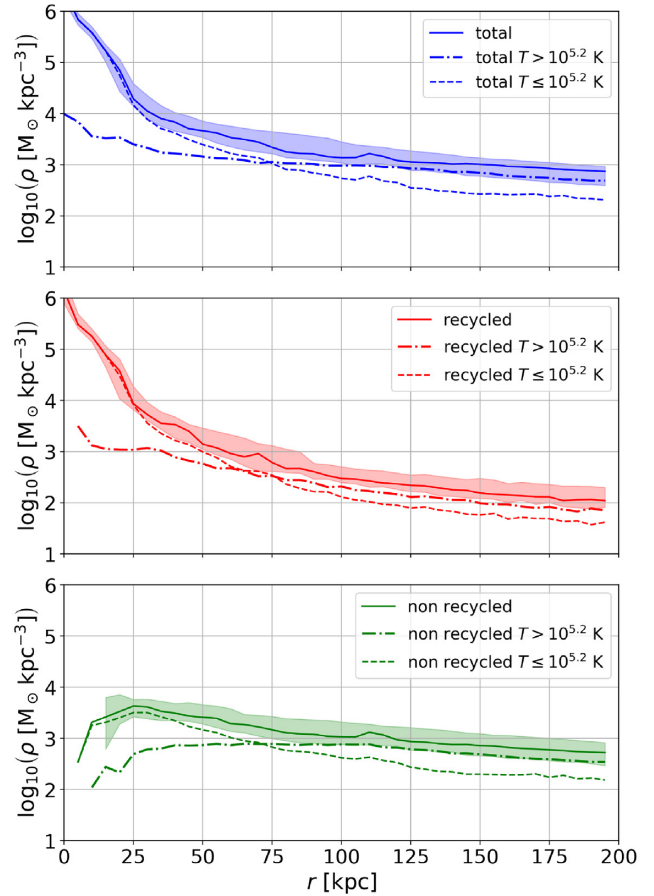


Figure 6. Average radial distribution of CGM gas for all simulated galaxies separated by temperature at $10^{5.2}$ K at $z = 0$. The top panel shows all gas, which is dominated by cooler gas at the central 75 kpc. In the middle and bottom panels, gas is split by its origin either recycled by the central galaxy (red lines) or accreted on to the halo without ever being in the ISM throughout its past recycling (green lines). At radii larger than 50 kpc, the CGM gas is dominated by accreted non-recycled gas which might have been enriched in other galaxies before infall.

To account for self-shielding, we follow the procedure outlined in Rahmati et al. (2013) to compute the effective attenuation of the ionizing background in dense gas. This ionizing background is then used in Cloudy to re-calculate the H I fraction. The fraction of molecular hydrogen (H_2) is not calculated, but at the impact parameters we consider the molecular fraction is not expected to be significant.

Metal lines are also impacted by self-shielding. The same attenuation factor for the ionizing background is used to recompute metal absorbers. This is not strictly accurate, as self-shielding likely changes the shape of the background, which is not accounted for. Self-shielding tends to only affect low ions such as Mg II, and even then fairly mildly. Neutral ions like Mg I would be more strongly impacted, but we do not consider such ions here since they are not typically seen in CGM absorption studies. Hence, our approximation is relatively robust, and follows that used in previous such studies (e.g. Ford et al. 2016).

Table 1 shows the size of the H I disc, computed as the radius at which the face-on radial surface density profile of H I drops below $1 \text{ M}_\odot \text{ pc}^{-2}$ (Wang et al. 2014). These values are broadly comparable to observations, but show a larger scatter than observed.

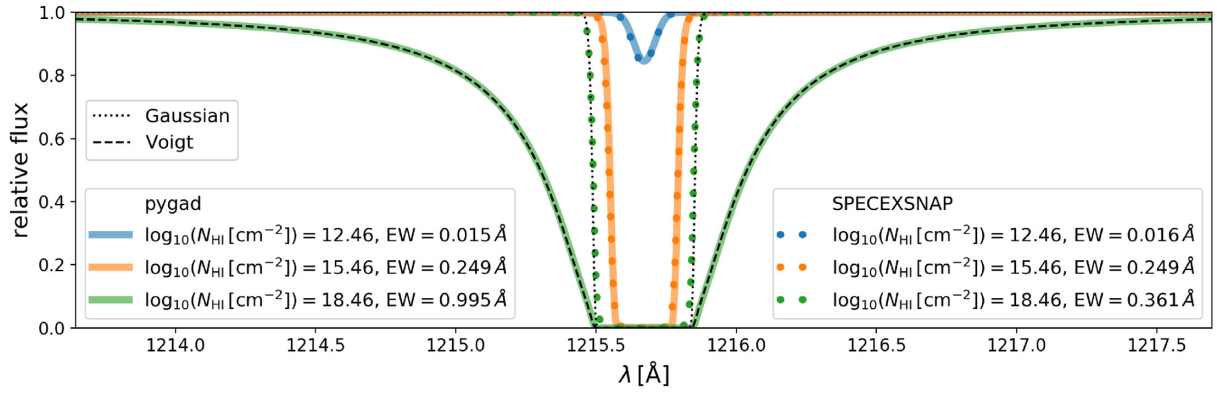


Figure 7. Comparison of the line profile generation from PYGAD (coloured lines) and SPECEXSNAP (coloured dots) from an idealized setup containing a cold blob of homogeneous gas with varying column densities (different colours) in a hot environment. The difference between a Gaussian profile (SPECEXSNAP, black dotted) and a Voigt profile (PYGAD, dashed lines) becomes clearly visible at the highest column density (green).

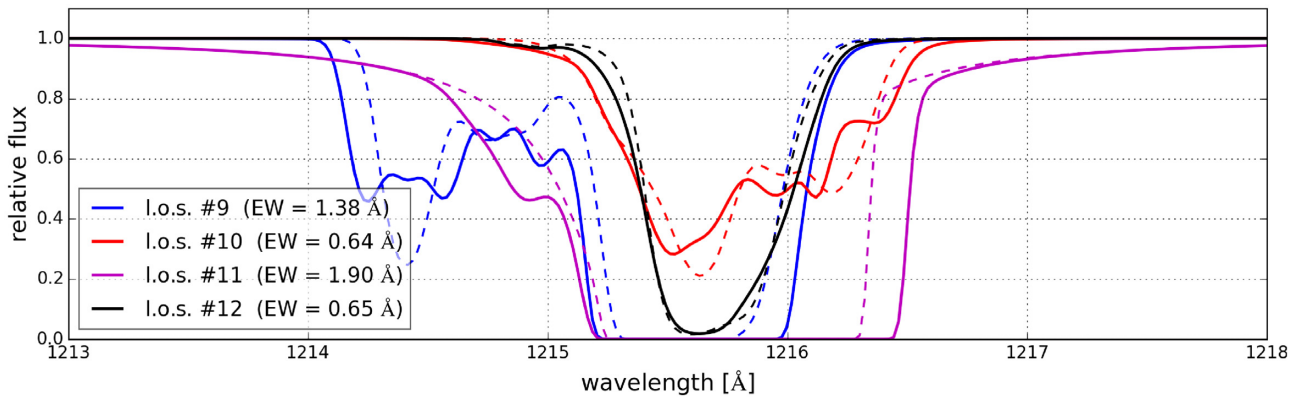


Figure 8. Mock Lyman α absorption spectra of M0858 for lines #9 through #12, cf. Fig. 9. Solid lines are generated by our fiducial method and the dashed lines by the smoothing first approach (cf. Section 4.2). Typically, the fiducial method results in boarder lines in the saturated regions and more substructure in the line wings. The EWs (#9 through #12) are 1.38 Å (1.14 Å), 0.64 Å (0.62 Å), 1.47 Å (1.14 Å), and 0.65 Å (0.61 Å) for the fiducial (smoothing first) method. For line #11, we can see damping wings.

4.2 Generating spectra from simulations

Techniques for generating mock spectra have been developed in numerous forms (e.g. Oppenheimer & Davé 2006; Hummels, Smith & Silvia 2017), but none so far have combined the features of being PYTHON-based, native-SPH, and computationally efficient. Hence, we develop and implement our own spectral generation code into our publicly available PYGAD package. Along the way, we explored several variants in the way to smooth gas elements on to the line of sight (LOS), in order to better understand uncertainties associated with mock spectrum generation.

To generate a spectrum for a particular ion, we (i) compute the ionization fraction of a given SPH particle; (ii) smooth the ion density on to the LOS via a gather approach at the LOS velocity of each pixel; (iii) convert the ion column density into an optical depth given the ion’s oscillator strength. This approach is used in e.g. the SPH-based spectra generation code SPECEXSNAP (Oppenheimer & Davé 2008).

To test this implementation and compare to SPECEXSNAP, we set up homogeneous spheres of cool dense ($T = 10^4$ K, $n_H = 0.1$ cm $^{-3}$) gas at fixed density and temperature embedded in hot low-density ($T = 10^6$ K, $n_H = 0.001$ cm $^{-3}$) ambient medium. The size of the sphere is varied to result in hydrogen column densities of 10^{13} , 10^{16} , and 10^{19} cm $^{-2}$, respectively. Due to partially ionized hydrogen,

the H I column densities are about 0.5 dex lower. These cases cover the linear, exponentiallogarithmic, and square-root regimes of the curve of growth for H I (see Section 5.4). In Fig. 7, we compare the two codes. For the two low column density cases (blue and orange) the results are identical. At the highest column density, the natural line width dominates the profile which is perfectly captured by PYGAD when compared to the theoretical Voigt profile (black dashed line). SPECEXSNAP is limited to Gaussian line generation (black dotted line).

Another approach is to smooth the physical quantities on to the LOS first, and then compute the ionization fraction from those smoothed physical quantities (e.g. binning data on a grid). In effect this switches steps (i) and (ii) in the above procedure. This is generally not preferred because particles with significantly different physical conditions (e.g. temperatures) can legitimately be regarded as representing multiphase gas, in particular in the simulation approach followed here. Averaging the physical properties removes this multiphase nature, and creates ionization fractions that reflect an average of multiple phases. To compare these approaches, we have implemented both methods into PYGAD.

Fig. 8 shows example absorption Lyman α spectra of halo M0858 for four selected lines of sight with both methods (for the location of each LOS see Fig. 9). The solid spectra are generated with

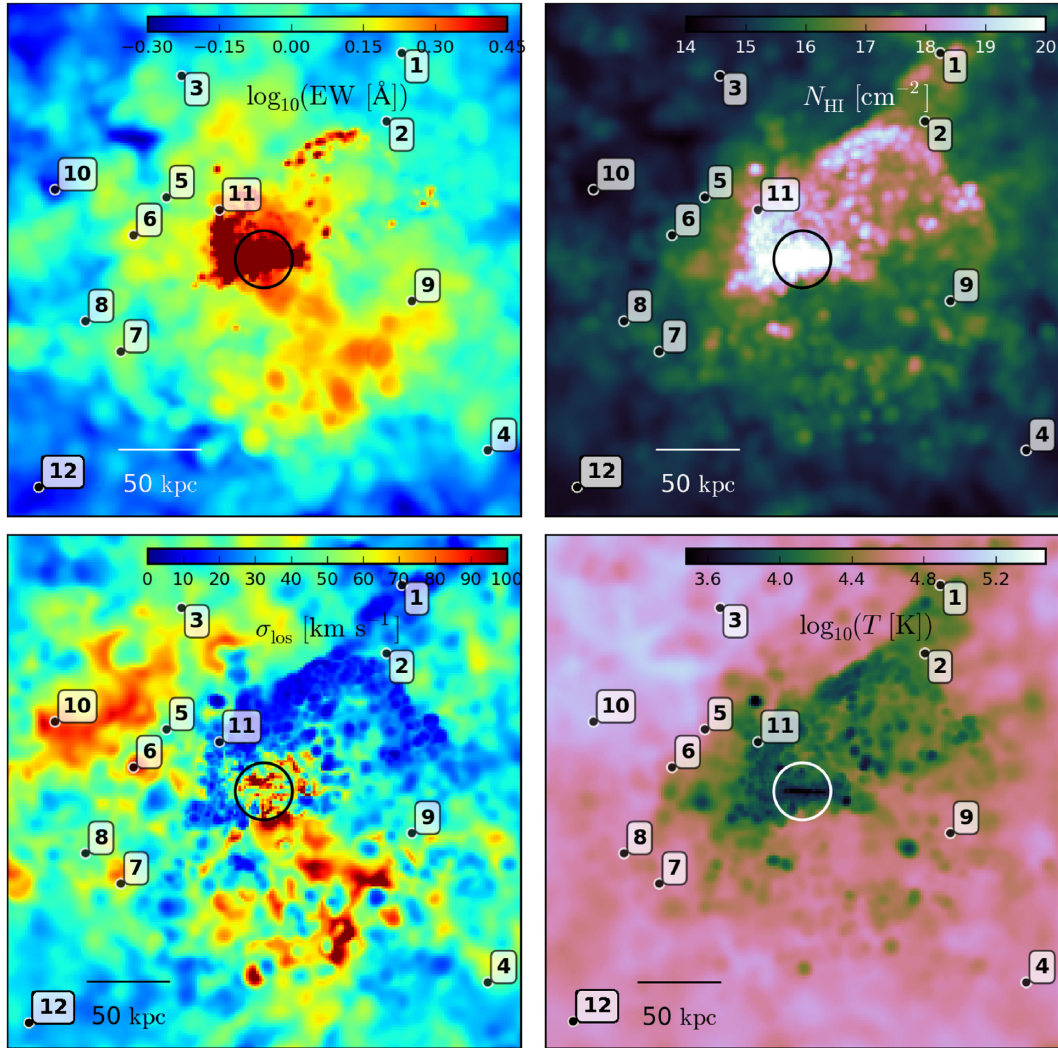


Figure 9. Projection of M0858 in a region 306 kpc on a side. We show the Lyman α EWs (upper left), column densities of H I (upper right), the H I gas velocity dispersion (bottom left), and the mean H I mass weighted gas temperature (bottom right). EWs in the densest regions ($\gtrsim 10^{15} \text{ cm}^{-2}$, logarithmic regime) do not change significantly with column density, but mostly with LOS velocity structure. The sample spectra of Figs 8, 11, and 12 are indicated with numbers next to them.

our fiducial method, while the dashed spectra are generated by first smoothing the physical quantities. The general trend is that the fiducial method shows larger equivalent widths (EWs), often by 20 per cent or more, possibly due to a better representation of the broadening by LOS velocity. These spectra were chosen to emphasize the difference between the methods, especially lines #9 and #10. More typical spectra are shown in Figs 11 and 12. Line #11, is a common example, where an additional absorption feature occurs next to the main feature and causes it to become significantly wider. This shows that, in some cases, the choice of exactly how to generate mock spectra can result in mild but non-zero differences in the resulting column densities.

5 HALO ABSORPTION PROPERTIES

We now examine the absorption properties of CGM gas in our zoom suite. While we will compute statistics from our full sample, Halo M0858 will continue to serve as an example throughout the work, since it is fairly typical and contains a variety of interesting features.

5.1 CGM absorption structure

For halo M0858 we create a regular grid of 200×200 equally spaced sightlines along the x -axis. For each sightline we generate a mock Lyman α spectrum with our fiducial method and calculate the corresponding EW. Fig. 9 shows the 306 kpc per side map of EW (top left), H I column densities (top right), the H I LOS velocity dispersion (bottom left), and the mean H I-mass weighted temperatures (bottom right). The properties of the highlighted 12 lines-of-sight are summarized in Table 3.

On large scales, the structure of the EW map is well correlated with the column densities. There is a dense central region hosting the main galaxy, an accretion flow from the upper right that is evident as a low-temperature, low-dispersion extension, and an outflow above and below the (horizontal) disc as particularly evident from the larger velocity dispersion.

Looking more closely, discrepancies between the EWs and the column densities emerge, particularly in the regions of the inflow and outflow. While the densest knots are apparent in both high column and EW, absorption at $N_{\text{H I}} \sim 10^{18} \text{ cm}^{-2}$ particularly along

Table 3. The properties of the chosen lines: the column density N , the equivalent width EW, velocity dispersion σ , and impact parameter ρ . The spectra are shown in Figs 8, 11, and 12 and the actual positions are indicated in Fig. 9.

Number	$\log_{10}(N)$ (cm^{-2})	EW (\AA)	σ (km s^{-1})	ρ (kpc)
1	16.46	0.982	19.5	147.3
2	16.35	0.968	33.5	110.0
3	14.72	0.903	51.3	120.1
4	14.85	0.948	44.8	175.5
5	15.55	1.136	41.7	68.1
6	15.64	1.535	92.9	79.0
7	15.55	1.278	63.9	101.3
8	15.34	0.889	44.6	112.8
9	15.96	1.379	38.7	92.0
10	14.22	0.636	81.4	130.3
11	18.66	1.897	22.7	40.3
12	14.47	0.651	30.3	185.0

the accreting filament are not obvious as high-EW structures. Conversely, the outflow to the lower right shows higher EWs, with no corresponding features in the column density. This indicates local dynamical effects can complicate the association between column density and EW.

To explore this more quantitatively, we show in Fig. 10 scatter plots of EW versus $N_{\text{H I}}$ (left-hand panel), the mass weighted LOS velocity dispersion σ_{los} (middle), and the temperature T (right), for all the lines of sight. In the left-hand panel, the points are colour coded by the σ_{los} , while in the other two panels they are colour coded by $N_{\text{H I}}$.

While there is a general trend of higher EW corresponding to higher $N_{\text{H I}}$, there is a substantial scatter in EW at a given column density. Moreover, this scatter correlates well with σ_{los} . This is not surprising, since saturated lines can be broadened by both enhanced columns and by enhanced velocity broadening. However, it is notable that at the highest columns, the trend is fairly tight with EW, as the dispersion tends to be quite low along these LOS.

The low dispersion at high columns is also evident in the middle panel, where the strongest lines appear at the lowest $\sigma_{\text{los}} \approx 10\text{--}20 \text{ km s}^{-1}$. For the weaker lines there is no strong correlation between absorption strength and LOS dispersion, though there is a weak trend that the highest dispersions create somewhat larger EWs, as might be expected from line broadening.

The strong lines with low σ_{los} also correspond to gas with the lowest temperatures, typically $T \approx 10^4 \text{ K}$. Since this corresponds to a Gaussian velocity dispersion of around 9 km s^{-1} , it explains why no σ_{los} values are seen below this. Moving to the weaker absorbers, the temperatures tend to be higher. In Section 5.4 we discuss in detail how the CGM motion along the LOS affects the EW, in addition to the thermal line broadening.

For further analysis we marked lines with similar EW ($\sim 0.95 \text{ \AA}$) and column densities varying by about two orders of magnitude as #1 through #4 (see Figs 9 and 10). The line profiles are shown in Fig. 11. Naively, higher column densities would result in higher EWs. However, this trend is compensated by lower temperatures and lower LOS velocity dispersion (see middle and right-hand panels of Fig. 9). EW increase due to higher column density is compensated by a lower b -parameter and a lower LOS dispersion resulting in lines #1 to #4 lining up almost horizontally in the left-hand panel of Fig. 10.

Lines of sight with very similar column densities of about $\sim 10^{15.6} \text{ cm}^{-2}$ but strongly varying EWs are highlighted in #5 through #8 (Fig. 12). Line #8 has the lowest EW of 0.90 \AA with a velocity dispersion of $\sim 45 \text{ km s}^{-1}$, whereas line #6 has an EW of 1.53 \AA and a $\sigma_{\text{los}} \sim 100 \text{ km s}^{-1}$. This is an example where higher velocity dispersion generates larger EW at similar column density, with lines #5 to #8 lining up vertically in the left-hand panel of Fig. 10.

5.2 Individual line profiles

The gas velocity structure along each LOS can play an important role for the determination of EWs at the disc–halo interface, where the Lyman α column densities are in the logarithmic regime of the curve of growth. In our simulations this regime stretches out to a few H I disc sizes, almost reaching the R_{200} of our galaxies. Here, we examine some individual LOS to see how they reflect the underlying CGM physical conditions.

The line spectra of the already discussed sightlines are plotted in Fig. 11 (#1 to #4), Fig. 12 (#5 to #8), and Fig. 8 (#9 to #12). The lines have impact parameters between $2 R_{\text{H I}}$ and $11 R_{\text{H I}}$ at H I column densities of 10^{14} to 10^{17} cm^{-2} , and one at 10^{19} cm^{-2} . Most lines are saturated at EWs higher than 0.8 \AA , the only exceptions being lines #10 and #12 with EWs of $\sim 0.6 \text{ \AA}$. Due to the saturation, the Lyman α absorption lines do not show clear internal structure. This makes it impossible to distinguish between line broadening by

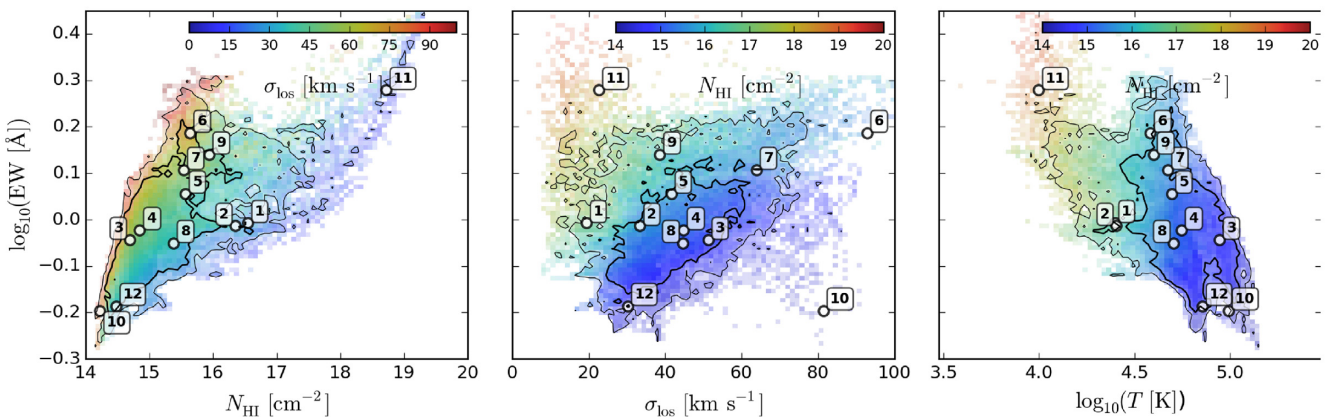


Figure 10. Correlations of EW with column density, LOS dispersion, and temperature for the maps in Fig. 9. Special lines of sight are numbered and discussed in the text.

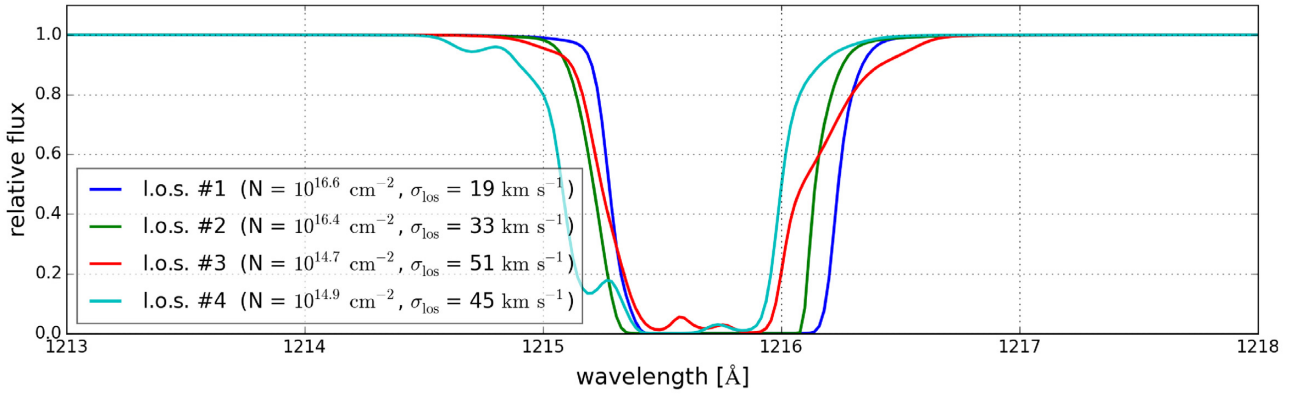


Figure 11. Lyman α absorption spectra for lines #1 through #4 as marked in Fig. 9 (cf. also Fig. 10). The lines have similar EWs $\sim 0.95 \text{ \AA}$, but different LOS velocity dispersions. In general, the broadening due to LOS dispersion/velocity effects cannot be identified as the lines are saturated. For a few cases, like line #4, weak separate lines can appear (at $\sim 1215.1 \text{ \AA}$).

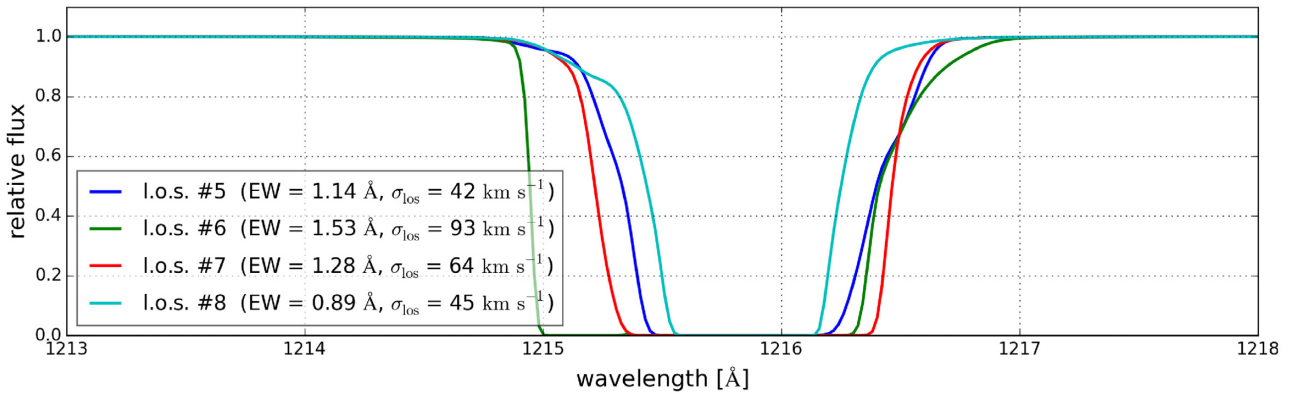


Figure 12. Lyman α absorption spectra for lines #5 through #8 as marked in Fig. 9 (cf. also Fig. 10). All lines have similar column densities of about $10^{15.6} \text{ cm}^{-2}$, but varying EWs due to their different LOS velocity structure.

column density, temperature b -parameter (line #3) or LOS velocity structure (line #2).

Only in a few cases (lines #9 and #10) do we see more complex line shapes, often generated by several resolved lines. A solid physical interpretation of these structures from simulations in general is difficult, both because the interpretation can change with the method to generate the lines. Here, we highlight one line which is not saturated and allows for a detailed physical interpretation of the complex line shape. While this cannot be generalized it nevertheless indicates how simulations can support the analysis of complex line shapes. In Fig. 13, we show the distribution of the H I column density in LOS velocity along the sightline #9 (x -axis), as an example. It covers 400 kpc and about 400 km s^{-1} in velocity space. Alongside the total spectrum we show spectra of gas in the marked (blue and green) regions artificially separated in velocity space. Most of the mass is at LOS positions between $x = 0 \text{ kpc}$ and $x = 100 \text{ kpc}$ with absolute velocities of less than 100 km s^{-1} . This corresponds to a total shift of about 0.4 \AA , a bit less than its EW. Towards negative positions we find gas with LOS velocities down to $\sim 300 \text{ km s}^{-1}$, explaining the $\sim 1 \text{ \AA}$ wide wing in the spectrum towards shorter wavelengths.

5.3 Radial equivalent width profiles

By combining single LOS observations around a suite of galaxies, it is possible to characterize the typical absorption profile in the CGM.

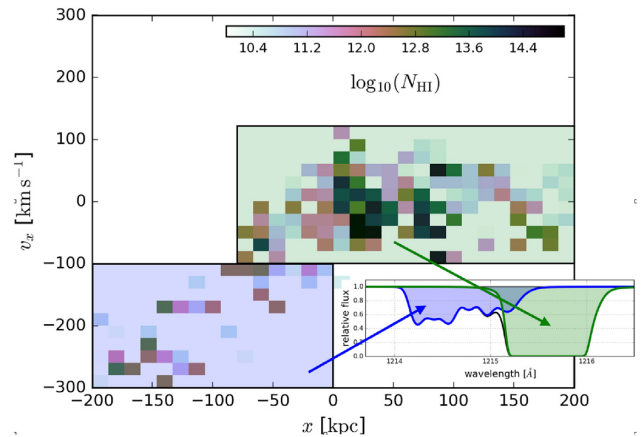


Figure 13. The column density distribution along the LOS number 9 (cf. Figs 8, 9, and 10) and as a function of its velocity v_x and position x along the LOS. In the 2D histogram, the amount of column density in each pixel is colour coded. In the inlayed spectrum of the line (cf. Fig. 8), we separated the H I mass by its position and velocity as indicated by the coloured regions in the phase space and created spectra of just that mass. The mass extending towards negative positions and velocities (light blue square) created the left wing (also light blue) in the spectrum, whereas the rest creates the main line.

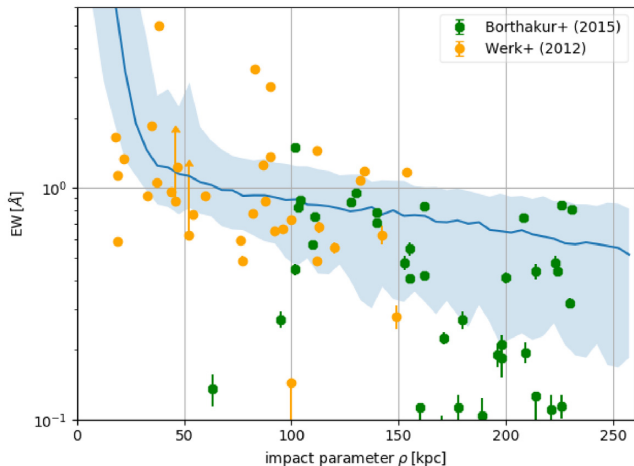


Figure 14. The EWs of the Lyman α lines for all haloes in edge-on projection as a function of their impact radius ρ . The green points are observational from Borthakur et al. (2015) and the orange from Tumlinson et al. (2013).

As an example, the COS-GASS survey (Borthakur et al. 2015) selected galaxies having H I data, and found a clear correlation of more gas-rich galaxies (as seen in 21 cm emission) having higher H I EW absorption. Here, we compare our suite of simulations to the H I absorption as a function of impact parameter from these data.

Fig. 14 shows the average radial H I EW profiles of all our seven galaxies without a (major) merger (see also Table 1) out to several H I disc sizes. The M0858 halo is plotted to larger radii. Overplotted are observations from the GASS, GBT, CHA, and ALFALFA surveys as taken from Borthakur et al. (2015).

The simulated radial profiles follow the observed trends reasonably well, both in amplitude and trend. This is in agreement with results from Gutcke et al. (2017), who compare H I surface density profiles from the NIHAO zoom simulations to H I column densities inferred from simulations. There is a lack of low-EW absorption seen in our simulations, indicating somewhat more absorption than typically observed. A partial explanation might be found in survey selection, as the observations have a median stellar mass of $10^{10.4} M_{\odot}$, H I mass of $10^{9.4} M_{\odot}$, and disc size R_{HI} of 16.2 kpc, whereas our sample chosen solely by mass has a median stellar mass of $10^{10.8} M_{\odot}$, an H I mass of $10^{10.0} M_{\odot}$ and a disc size R_{HI} of 25 kpc. Hence, our simulated galaxies are somewhat larger, potentially giving rise to higher EW. None the less, the general predicted trend of a broad range of CGM absorption strengths as a function of impact parameter is broadly consistent with observations.

5.4 EW versus column density profiles

In Fig. 15, we show four examples for curves of growth relating column density to EW for Lyman α with b -parameters of 2025, 50, 75, and 100 km s^{-1} . In the linear regime at low column densities ($\log N_{\text{HI}} \lesssim 14$), the line is optically thin. At higher column densities the line becomes saturated (linear or logarithmic regime), and at higher column densities it is dominated by the outer Lorentzian wings of the natural line broadening (square-root regime at $\log N_{\text{HI}} \gtrsim 19$). Most CGM Lyman α absorbers are in the logarithmic regime of the curve of growth where changes in column density do not affect EWs strongly. As the thermal b -parameter for $T = 10^4 \text{ K}$ gas is only $\sim 13 \text{ km s}^{-1}$ we expect the broadening to be dominated by CGM kinematics. By comparing the EW and

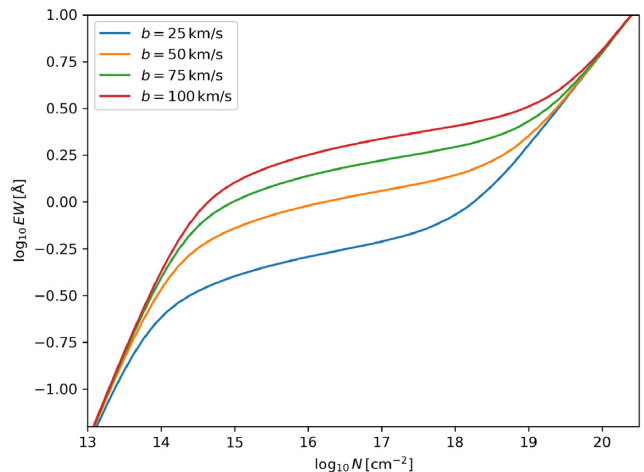


Figure 15. Four example curves of growth (COG) for Lyman α with b -parameters of 2025, 50, 75, and 100 km s^{-1} .

column density radial profiles from the simulations we can derive an effective b -parameter which might be useful to convert observed Lyman α EWs to column densities.

In the left-hand panel of Fig. 16, we show the simulated column density distribution (green dashed line) and the EW distribution derived with PYGAD by including all absorption along the LOS (orange line). A remarkably good match (blue line) to the this EW distribution can be obtained assuming a single COG with an effective b -parameter of $b = 62 \text{ km s}^{-1}$ when converting column densities to EWs. In the right-hand panel of Fig. 16, we show that such an optimal b -parameter is almost independent of radius (orange line). Here, the b -parameter has been determined at each radial distance from finding the optimal COG (see Fig. 15) resulting in the smallest rms difference between the COG inferred EW and the EW from the PYGAD analysis. The optimal b -parameter is clearly higher than the Doppler parameter for simple thermal broadening of hydrogen $b = \sqrt{k_B T / m_{\text{ion}}}$ (blue line in Fig. 15). This indicates that velocity broadening is dominating the EWs of these absorbers.

We conduct an analogous analysis for all other haloes. They consistently show an optimal b -parameter that has very little variation with radius. However, the values of the b -parameters change with halo mass and for lower mass haloes the contribution from the thermal broadening is more significant.

Fig. 17 shows the mean optimal b -parameter with standard deviation in the radial range from 50 to 250 kpc for all haloes as a function of their mass. We see a clear trend of the optimal b -parameter increasing with halo mass. The correlation is worse with stellar mass, gas mass, or baryonic mass. The exponential fit to the data is

$$b_{\text{optimal}} = \left(\frac{M_{200}}{10^{12} M_{\odot}} \right)^{0.132} 58.1 \text{ km s}^{-1}. \quad (9)$$

We note that low-redshift observational CGM studies have typically assumed b -parameters in the range of $25\text{--}30 \text{ km s}^{-1}$ when converting from EW to column density (e.g. Werk et al. 2014). This is generally well below the values suggested by our simulations. Hence, the observationally inferred column densities may be significantly overestimated, which could also affect the inferred halo baryon budget. We would like to point out that observations indicating higher b -parameters (see Borthakur et al. 2016, fig. 6) are consistent with our findings and a trend with halo mass is not seen.

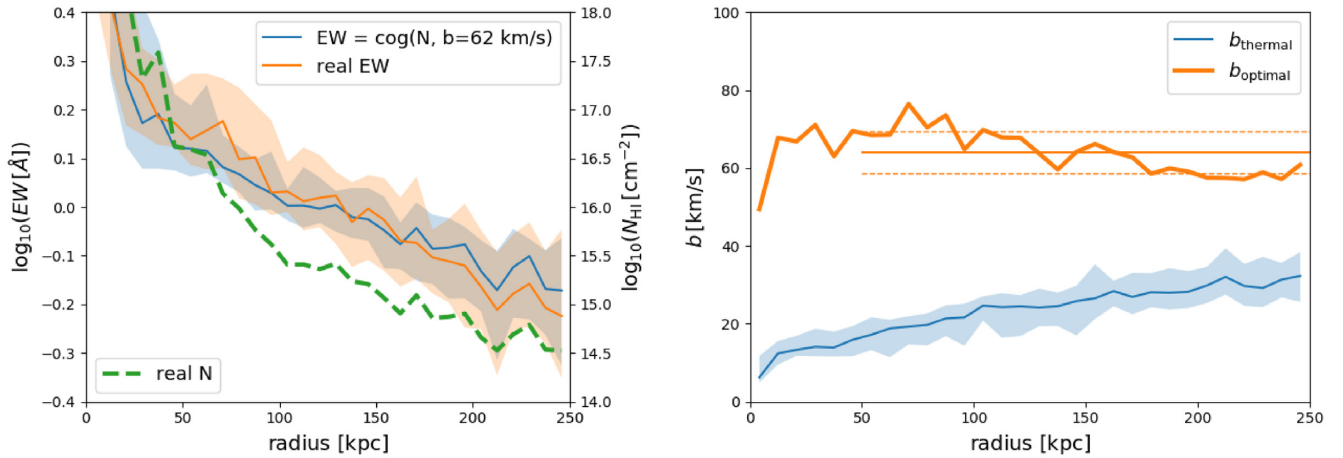


Figure 16. Radial profiles of EW and column density for M0858 in edge-on projection on the left with arbitrary matching of the scales. EWs as obtained by the mock line spectra (orange line) with the shaded region indicating the 10th and 90th percentile. The simulated column densities (green line), omitting the scatter for better visibility (note: full transition into logarithmic region is at $\sim 10^{15} \text{ cm}^{-2}$). EW calculated from the LOS column densities and assuming a COG with $b = 62 \text{ km s}^{-1}$ (blue line) with the shaded region indicating the 10th and 90th percentile. The right-hand panel shows the thermal b -parameters as a function of radius (blue line) and the ‘optimal’ b -parameters (orange line) for M0858. This ‘optimal’ b -parameter is the value for which the rms of difference between the (logarithmic) EWs obtained from a COG and the actual EWs is the smallest. The solid horizontal line indicates the mean over this radial range and the dashed lines the rms.

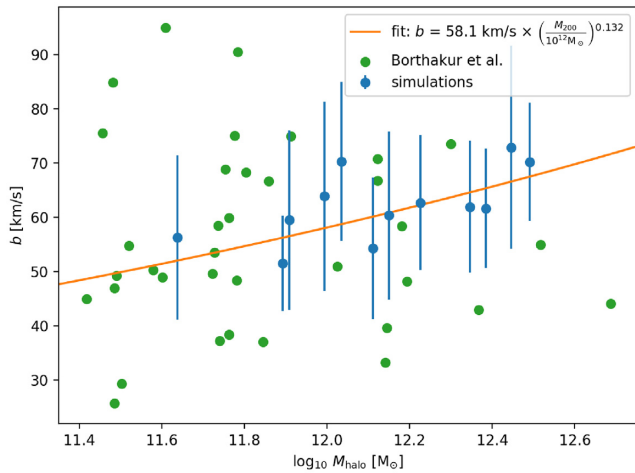


Figure 17. The ‘optimal’ b -parameters (cf. Fig. 16 and the text) over the radial range 50–250 kpc in edge-on projections as a function of halo mass for all simulated galaxies. The error bars show the standard deviations of the optimal b -parameters. The data was fitted with an exponential function: $b = b_0 [M_{200}/(10^{12} M_{\odot})]^x$ with a best fit of $b_0 = 58.1 \text{ km s}^{-1}$ and $x = 0.132$. For M0858 ($M_{\text{halo}} = 10^{12.23} M_{\odot}$) this results in $b = 62 \text{ km s}^{-1}$ as used in Fig. 16. Data taken from Borthakur et al. (2016).

5.5 Angular dependence of the equivalent widths

We investigate the angular trends of Lyman α EWs which can be difficult to access with observations. The canonical view is that gas falling into the halo preferentially arrives in the disc plane, while outflows of generally hotter (enriched) gas are perpendicular to the disc. Hence, higher EWs are expected in the disc plane relative to perpendicular to the disc.

Fig. 18 shows the deviation of the EW from the radial average as a function of angle from the disc plane. We find two classes of objects. The first class are galaxies with clear signs of recent interactions or mergers show no correlation of EW variations with polar angle. These are simulations M0664, M0858, and M228, which are shown

in the upper panels of Fig. 18. Dense gas orbiting in the halo, also with increased velocity dispersion can result in elevated EWs at all polar angles at all radii. The typical effect of a minor merger or accretion event can be seen in M0858 (Fig. 9). Note that a merger can disturb the system for a long time. For M1859 (Fig. 19), the last minor merger happened more than 5 Gyr ago.

The second class of objects are galaxies in quiet environments like M0501, M0959, and M1196 (bottom panels of Fig. 18). They show clear correlations with polar angle, displaying high column densities extending to large radii well beyond the H I disc. Hence, in our simulations, galaxies must have experienced a very quiet merger history for a long time preceding observation in order to display a clear azimuthal signal of H I EW with position angle.

6 FEEDBACK AND RESOLUTION DEPENDENCE

To test the sensitivity of our results to variations in resolution and input physics, we run two additional simulations of Halo M1859. In the first, the ‘8x’ run, we increase the mass resolution by a factor of 8 relative to our fiducial 4x run. We also run a weak feedback model (weakFB) where we reduce the outflow velocity in SNe from 3000 km s^{-1} to just 30 km s^{-1} , reducing the input of momentum into the surrounding gas, which increasing the thermal energy input to maintain 10^{51} erg per SN. We note that this run does not reproduce basic observations such as the stellar-to-halo mass ratio, but is still an instructive test case. Besides these changes, all physical modelling and analysis procedures are kept identical.

For the 8x run, the final halo properties are virtually identical to the 4x run: M_{200} drops by 2.6 per cent and R_{200} by 0.85 per cent relative to the 4x run. For the stellar mass, however, the differences are larger. The differences are larger when looking at the stellar and gas mass of the galaxy. Stellar mass increases by 8.6 per cent up to $1.72 \times 10^{10} M_{\odot}$, whereas the gas mass decreases from 9.09 to $4.37 \times 10^9 M_{\odot}$ (-52.2 per cent). H I mass similarly decreases from 5.87 to $2.76 \times 10^9 M_{\odot}$ (-53.1 per cent). The (mass-weighted)

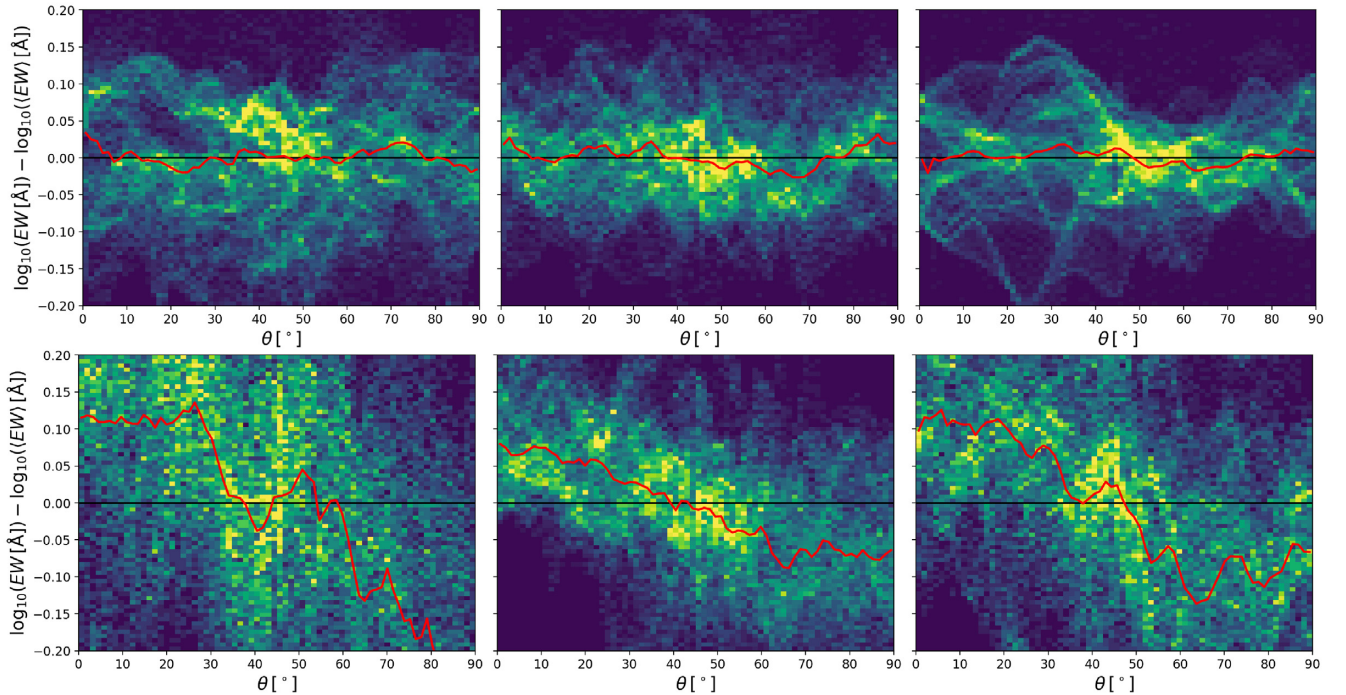


Figure 18. Deviations of the EWs from the mean EW at a given radius as a function of the polar angle (the angle to the disc) of the LOS in edge-on projections. Here, 0° is in the plane of the disc and 90° is perpendicular to the H I disc. The yellow colouring shows the density of LOS at that δ EW and position angle. The red line is the median deviation at a given angle. We find two classes of haloes: one without an angular dependence as is the case for M0664, M0858, and M2283 (upper row from left to right); and one with a clear angular dependence for which we show examples in the bottom row (from left to right: M0501, M0959, M1196).

average stellar ages are again very similar: 6.96 Gyr for the 8x run versus 7.02 Gyr for the fiducial 4x run. The drop in gas mass is much larger than the increase in stellar mass, showing that the gas has ejected substantially more gas. Hence, higher resolution tends to lock somewhat more mass into stars, but also blow out more gas.

The weakFB run shows much larger differences. First, the halo mass grows by about 10 per cent (and correspondingly, R_{200} by 3 per cent), demonstrating that feedback lowers the halo mass. The stellar mass increases by a factor of 4 to $6.74 \times 10^{10} M_\odot$, which shows that kinetic feedback from SN is crucial for regulating the conversion of gas into stars in the ISM. Meanwhile, the gas mass drops to $2.98 \times 10^9 M_\odot$, which is three times lower than the original run. This directly arises because much of the gas has been converted into stars. Hence, strong feedback is responsible for keeping galaxies gas rich.

Fig. 19 shows maps for H I column densities, Lyman α EWs, H I velocity dispersions, and temperature, for our three variants. The original 4x run is shown in the top row. The 8x run in the middle row shows finer structures, but not overall a large difference in the general properties of the CGM. However, the weakFB run shows dramatic differences, as the CGM is much emptier, to the point that single particle blobs of absorption become evident. This shows that feedback has a dramatic impact on the structure of the CGM in these simulations.

Fig. 20 shows, the correlations of the EWs with column density, velocity dispersion, and temperature for all the discussed runs of halo M1859 that correspond to the maps in Fig. 19, similar to the plots shown in 10.

The first column shows a curve of growth plot. Increasing resolution makes no strong change, but the weakFB run oddly

shows three arms in the COG. The lower arm corresponds to a single particle in the north-east corner of the maps in Fig. 19. The upper two arms have EWs similar to the other two simulations and also their temperatures are around 10^5 K.

We also see differences in the LOS velocity dispersion. Increasing the resolution for this halo results in lower σ_{los} in weaker systems, likely because these systems can now be resolved better. The temperatures (right-hand column) are also slightly lower, but this cannot explain the difference in the dispersions. The weakFB run, in contrast, shows a dramatically different velocity and temperature structure, as much of the CGM has little to no absorption, and the strong lines are all concentrated to within the dense ISM.

7 SUMMARY

We study the CGM 11 zoom-in cosmological simulations of individual galaxy haloes using an improved version of the SPH-based galaxy formation model of Aumer et al. (2013). We exclude four that have mergers in their central galaxies, leaving 7 with virial masses in the range of $M_{200} = 4 \times 10^{11} - 3 \times 10^{12} M_\odot$, and central galaxy stellar masses of $7 \times 10^9 - 1 \times 10^{11} M_\odot$, thus broadly consistent with the observed stellar-to-halo mass ratio; more properties are listed in Table 1. From these simulations we produced mock absorption line spectra for the Lyman α transition, using a new module in our publicly available PYTHON package PYGAD, following SNAPEXBIN/SNAPEXSNAP (Oppenheimer & Davé 2006; Davé et al. 2010). We study general characteristics of the CGM in these haloes, and examine how Lyman α absorption traces the physical and kinematic conditions of the CGM gas in these simulations. Our main conclusions are as follows:

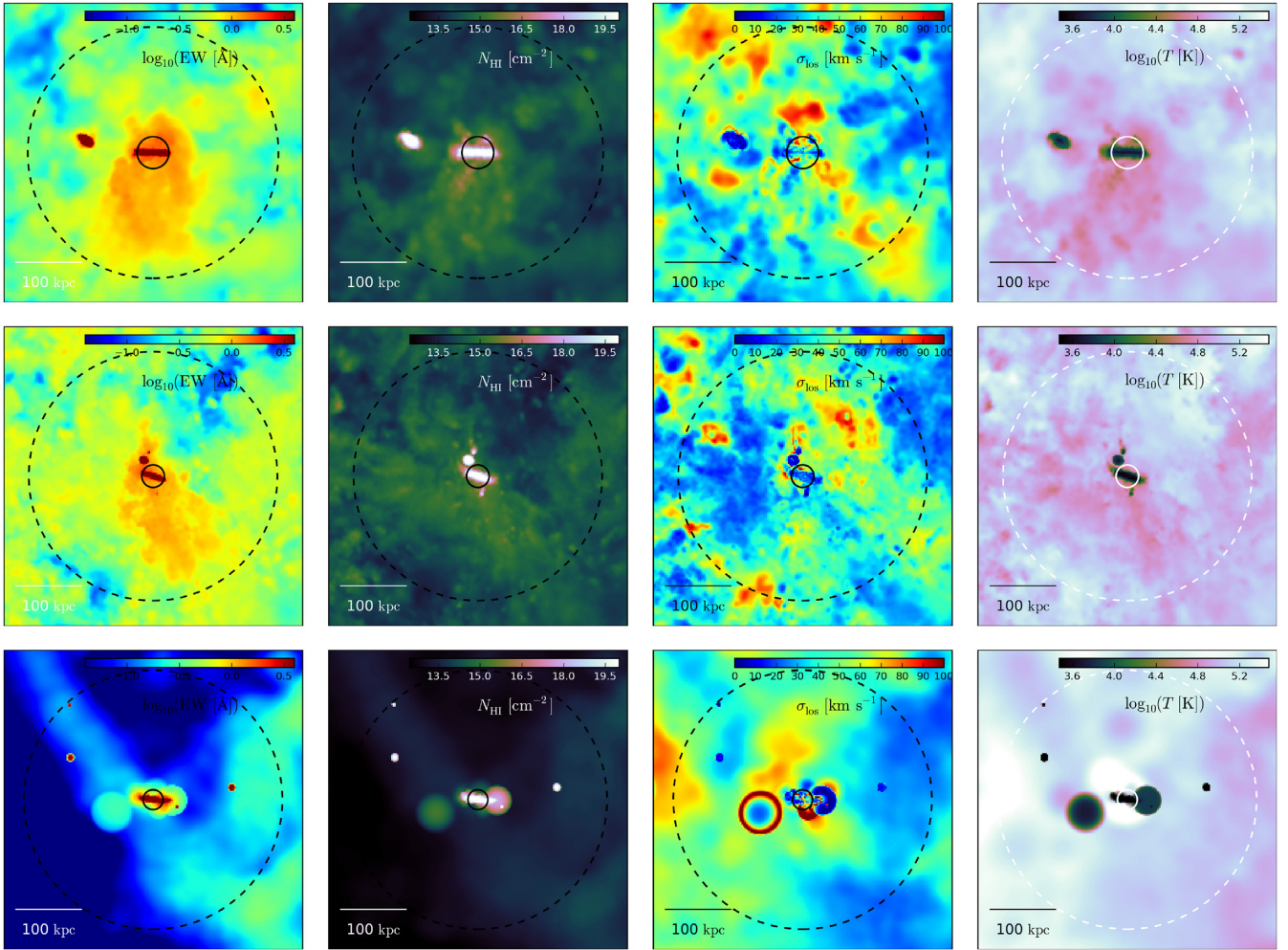


Figure 19. The maps of EW, hydrogen column density, LOS dispersion, and temperature (from left to right) for M1859 at the standard resolution (top row) and at a factor 8 higher mass resolution (middle row). The simulation with weaker feedback at standard resolution is shown at the bottom row. Here, the galaxy is almost devoid of a CGM as there is no gas recycling.

(i) We find that our haloes typically contain 50 per cent of their cosmic baryon fraction. This is roughly divided equally between disc (ISM) gas, cool CGM gas, and warm-hot CGM gas.

(ii) Halo accretion provides at least two-thirds of the CGM mass, and mass expelled from the ISM the remainder. This is qualitatively consistent with Hafen et al. (2020). At the present day, the rate of injection from these two sources is comparable.

(iii) Most CGM gas that is cold ($T < 10^{5.2}$ K) was accreted on to the halo, and the majority of that in cold form. ISM injected gas retained in the CGM was mostly injected hot.

(iv) Accreted CGM gas dominates at radii larger than 50 kpc, while recycled gas, gas expelled from the host galaxy ISM, dominates at smaller radii. The majority of CGM gas is accreted and not recycled within the host halo.

(v) We find that the exact procedure for generating absorption lines from SPH particles can significantly impacts the results, particularly in saturated CGM absorbers, with differences of up to 20 per cent in EW.

(vi) Bulk motions provide a significant contribution to the EW of typical CGM absorbers, because they tend to lie in the logarithmic portion of the curve of growth.

(vii) The strongest absorbers ($N_{\text{HI}} \gtrsim 10^{18} \text{ cm}^{-2}$) tend to arise in 10^4 K gas with low dispersion.

(viii) The mean EW drops with increasing impact parameter, in rough agreement with observations though with a hint of too much absorption at large radii.

(ix) Galaxies that experienced mergers show no azimuthal trend in EW, while galaxies that have had no mergers for at least 5 Gyr show significantly more absorption along the disc major axis and less along the minor axis.

(x) By comparing the EW and column density profiles, we find that CGM Lyman α absorbers are best represented by a radially constant b value that increases with halo mass, from 50 to 70 km s^{-1} across our halo mass range. These values are larger than typically assumed but are consistent with Borthakur et al. (2016).

(xi) Our results are somewhat sensitive to resolution, with significantly less ISM gas in a higher resolution test case. Our results are highly sensitive to feedback, as a run without feedback shows a dramatically different CGM that is strongly discrepant with observations.

In order to observationally disentangle the three main factors that contribute to the width of a typically saturated CGM Lyman α line (column density, H I temperature, and LOS velocity) additional information beyond the Lyman α line and its shape is needed. One

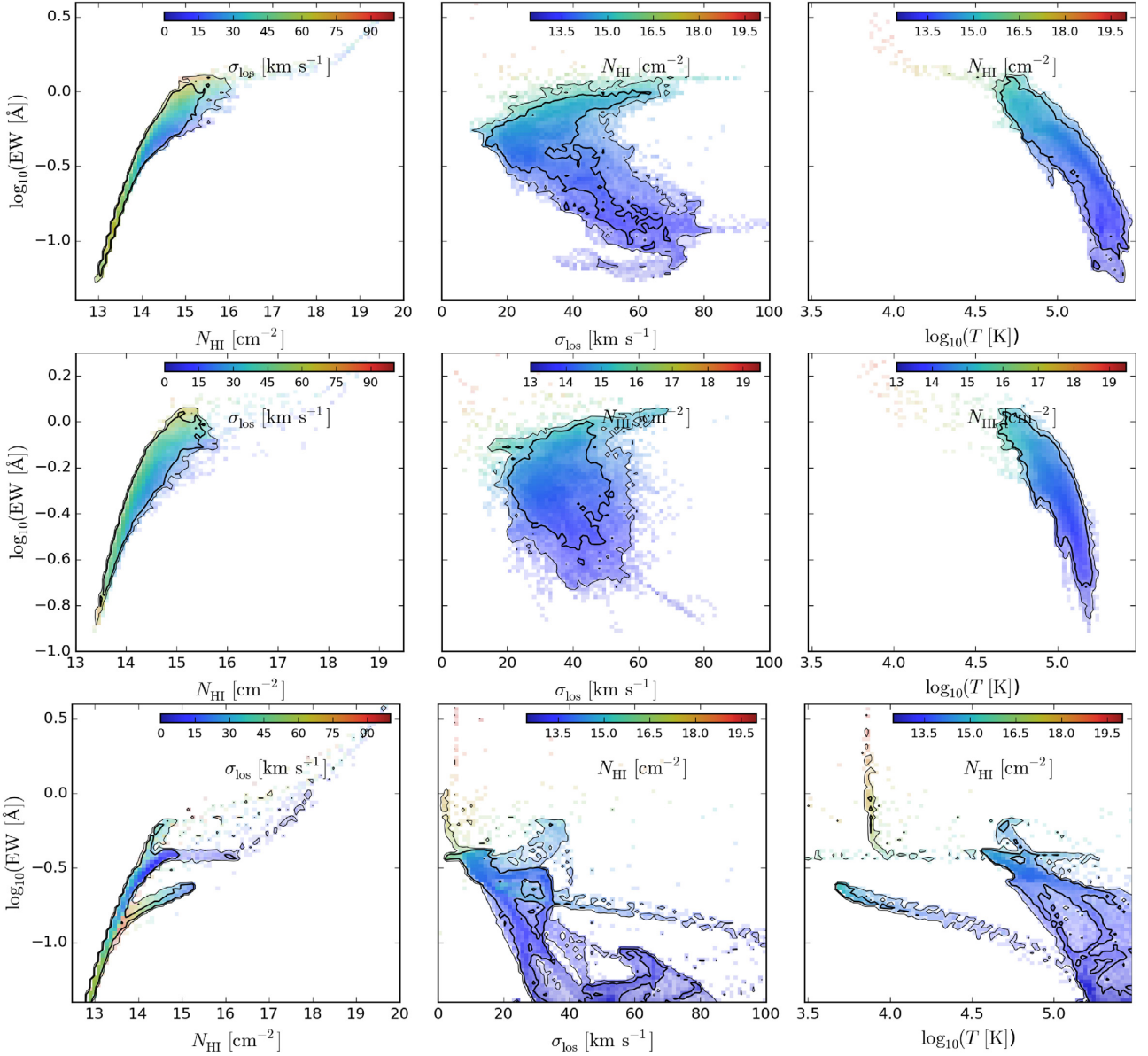


Figure 20. The maps for M1859 with our standard model and resolution (upper left panel), with increased resolution (initial particle masses are larger by a factor of 8; upper right), and with the standard resolution but a weaker feedback.

possibility is to look into the metal lines, which are usually not saturated. Churchill et al. (2015) found that low-ionization lines as such from Mg II $\lambda 2796$ are needed for this purpose as higher ionization lines such as C IV $\lambda 1548$ and O VI $\lambda 1031$ originate from very distinct phases of the CGM. By combining information from multiple ions together with insights from simulations such as these, it will be possible to disentangle the various CGM phases, obtain a more complete census of halo baryons, and trace the baryon cycle directly via absorption line probes.

8 SOFTWARE USED

This work was made using NUMPY (Walt, Colbert & Varoquaux 2011), SCIPY (Virtanen et al. 2020), MATPLOTLIB (Hunter 2007), IPYTHON (Pérez & Granger 2007), and JUPYTER notebooks (Kluyver et al. 2016).

ACKNOWLEDGEMENTS

This research was supported by the German Federal Ministry of Education and Research (BMBF) within the German-South-African collaboration project 01DG15006 ‘Ein kosmologische Modell für die Entwicklung der Gasverteilung in Galaxien’. TN acknowledges support from the Deutsche Forschungsgemeinschaft (DFG, German Research Foundation) under Germany’s Excellence Strategy – EXC-2094 – 390783311 from the DFG Cluster of Excellence ‘ORIGINS’. We thank Neal Katz for the helpful discussions and the SPECEXSNAP/SPECEXBIN code which we took as a basis for the implementation into PYGAD.

REFERENCES

Anglés-Alcázar D., Faucher-Giguère C.-A., Kereš D., Hopkins P. F., Quataert E., Murray N., 2017, *MNRAS*, 470, 4698

- Aumer M., White S. D. M., Naab T., Scannapieco C., 2013, *MNRAS*, 434, 3142
- Aumer M., White S. D. M., Naab T., 2014, *MNRAS*, 441, 3679
- Bailin J., Steinmetz M., 2005, *ApJ*, 627, 647
- Behroozi P. S., Wechsler R. H., Conroy C., 2013, *ApJ*, 770, 57
- Borthakur S. et al., 2015, *ApJ*, 813, 46
- Borthakur S. et al., 2016, *ApJ*, 833, 259
- Chen X.-W., Lanzetta K. M., Webb J. K., Barcons X., 1998, *ApJ*, 498, 77
- Chieffi A., Limongi M., 2004, *ApJ*, 608, 405
- Churchill C. W., Vander Vliet J. R., Trujillo-Gomez S., Kacprzak G. G., Klypin A., 2015, *ApJ*, 802, 10
- Davé R., Oppenheimer B. D., Katz N., Kollmeier J. A., Weinberg D. H., 2010, *MNRAS*, 408, 2051
- Dekel A. et al., 2009, *Nature*, 457, 451
- Ferland G. J. et al., 2013, *Rev. Mex. Astron. Astrofis.*, 49, 137
- Ford A. B., Oppenheimer B. D., Davé R., Katz N., Kollmeier J. A., Weinberg D. H., 2013, *MNRAS*, 432, 89
- Ford A. B., Davé R., Oppenheimer B. D., Katz N., Kollmeier J. A., Thompson R., Weinberg D. H., 2014, *MNRAS*, 444, 1260
- Ford A. B. et al., 2016, *MNRAS*, 459, 1745
- Gerhard O. E., 1983, *MNRAS*, 202, 1159
- Greif T. H., Glover S. C. O., Bromm V., Klessen R. S., 2009, *MNRAS*, 392, 1381
- Gutcke T. A., Stinson G. S., Macciò A. V., Wang L., Dutton A. A., 2017, *MNRAS*, 464, 2796
- Haardt F., Madau P., 2001, in Neumann D. M., Tran J. T. V., eds, *Clusters of Galaxies and the High Redshift Universe Observed in X-rays*. p. 64
- Hafen Z. et al., 2019, *MNRAS*, 488, 1248
- Hafen Z. et al., 2020, *MNRAS*, 494, 3581
- Hopkins P. F., Quataert E., Murray N., 2011, *MNRAS*, 417, 950
- Hummels C. B., Smith B. D., Silvia D. W., 2017, *ApJ*, 847, 59
- Hummels C. B. et al., 2019, *ApJ*, 882, 156
- Hunter J. D., 2007, *Comput. Sci. Eng.*, 9, 90
- Iwamoto K., Brachwitz F., Nomoto K., Kishimoto N., Umeda H., Hix W. R., Thielemann F.-K., 1999, *ApJS*, 125, 439
- Karakas A. I., 2010, *MNRAS*, 403, 1413
- Kauffmann G., Borthakur S., Nelson D., 2016, *MNRAS*, 462, 3751
- Kauffmann G., Nelson D., Borthakur S., Heckman T., Hernquist L., Marinacci F., Pakmor R., Pillepich A., 2019, *MNRAS*, 486, 4686
- Kennicutt R. C., Jr, 1998, *ApJ*, 498, 541
- Kereš D., Katz N., Weinberg D. H., Davé R., 2005, *MNRAS*, 363, 2
- Kluyver T. et al., 2016, in Loizides F., Schmidt B., eds, *Positioning and Power in Academic Publishing: Players, Agents and Agendas*. IOS Press, p. 87
- Kravtsov A., Vikhlinin A., Meshcheryakov A., 2018, *Astron. Lett.*, 44, 8
- Kroupa P., 2001, *MNRAS*, 322, 231
- Marri S., White S. D. M., 2003, *MNRAS*, 345, 561
- Moster B. P., Naab T., White S. D. M., 2013, *MNRAS*, 428, 3121
- Naab T., Ostriker J. P., 2017, *ARA&A*, 55, 59
- Nelson D. et al., 2018, *MNRAS*, 477, 450
- Oppenheimer B. D., Davé R., 2006, *MNRAS*, 373, 1265
- Oppenheimer B. D., Davé R., 2008, *MNRAS*, 387, 577
- Oppenheimer B. D., Davé R., Kereš D., Fardal M., Katz N., Kollmeier J. A., Weinberg D. H., 2010, *MNRAS*, 406, 2325
- Oppenheimer B. D., Schaye J., Crain R. A., Werk J. K., Richings A. J., 2018, *MNRAS*, 481, 835
- Oser L., Ostriker J. P., Naab T., Johansson P. H., Burkert A., 2010, *ApJ*, 725, 2312
- Oser L., Naab T., Ostriker J. P., Johansson P. H., 2012, *ApJ*, 744, 63
- Peeples M. S., Pogge R. W., Stanek K. Z., 2009, *ApJ*, 695, 259
- Peeples M. S., Werk J. K., Tumlinson J., Oppenheimer B. D., Prochaska J. X., Katz N., Weinberg D. H., 2014, *ApJ*, 786, 54
- Peeples M. S. et al., 2019, *ApJ*, 873, 129
- Pérez F., Granger B. E., 2007, *Comput. Sci. Eng.*, 9, 21
- Portinari L., Chiosi C., Bressan A., 1998, *A&A*, 334, 505
- Power C., Navarro J. F., Jenkins A., Frenk C. S., White S. D. M., Springel V., Stadel J., Quinn T., 2003, *MNRAS*, 338, 14
- Rahmati A., Pawlik A. H., Raicevic M., Schaye J., 2013, *MNRAS*, 430, 2427
- Röttgers B., 2018, *Astrophysics Source Code Library*, record ascl:1811.014
- Scannapieco C., Tissera P. B., White S. D. M., Springel V., 2005, *MNRAS*, 364, 552
- Scannapieco C., Tissera P. B., White S. D. M., Springel V., 2006, *MNRAS*, 371, 1125
- Schmidt M., 1959, *ApJ*, 129, 243
- Shen S., Wadsley J., Stinson G., 2010, *MNRAS*, 407, 1581
- Somerville R. S., Davé R., 2015, *ARA&A*, 53, 51
- Springel V., 2005, *MNRAS*, 364, 1105
- Springel V., Hernquist L., 2002, *MNRAS*, 333, 649
- Stern J., Hennawi J. F., Prochaska J. X., Werk J. K., 2016, *ApJ*, 830, 87
- Thom C. et al., 2012, *ApJ*, 758, L41
- Tumlinson J. et al., 2011, *Science*, 334, 948
- Tumlinson J. et al., 2013, *ApJ*, 777, 59
- Tumlinson J., Peeples M. S., Werk J. K., 2017, *ARA&A*, 55, 389
- Übler H., Naab T., Oser L., Aumer M., Sales L. V., White S. D. M., 2014, *MNRAS*, 443, 2092
- van de Voort F., Springel V., Mandelker N., van den Bosch F. C., Pakmor R., 2019, *MNRAS*, 482, L85
- Virtanen P. et al., 2020, *Nat. Methods*, 17, 261
- Walch S. et al., 2015, *MNRAS*, 454, 238
- Walt S. v. d., Colbert S. C., Varoquaux G., 2011, *Comput. Sci. Eng.*, 13, 22
- Wang J. et al., 2014, *MNRAS*, 441, 2159
- Wang L., Dutton A. A., Stinson G. S., Macciò A. V., Gutcke T., Kang X., 2017, *MNRAS*, 466, 4858
- Werk J. K. et al., 2014, *ApJ*, 792, 8
- Wiersma R. P. C., Schaye J., Smith B. D., 2009, *MNRAS*, 393, 99

This paper has been typeset from a \LaTeX file prepared by the author.